submitted to Geophysical Journal International

A discrete fracture hybrid model for forecasting diffusion-induced seismicity and power generation in Enhanced Geothermal Systems

Dimitrios Karvounis[1] and Stefan Wiemer[1]

[1] Swiss Seismological Service, ETH Zurich, Sonneggstrasse 5, NO H 63, CH-8092 Zurich, Switzerland.

E-mail: karvounis@sed.ethz.ch

SUMMARY

We describe a three-dimensional discrete fracture hybrid model (DFHM) that returns forecasts of both induced seismicity and of power generation in an Enhanced Geothermal System (EGS). Our model considers pore-pressure increase as the mechanism driving induced seismicity, similarly to other hybrid models, but it employs discrete fracture modelling for flow and heat that allows accurate and realistic transient solutions of pore pressure and temperature in fractured reservoirs. Earthquakes and flow are thus considered as closely coupled processes. In the DFHM model, the creation phase of an EGS is described as a Markovian process with a transitional probability that encapsulates the irreducible uncertainty with regards to induced seismicity. We conditioned this transitional probability on field observations from the 2006 EGS project in Basel, achieving a good match with observations of seismicity evolution. Specifically, our model effectively reproduces and explains the observed long-term exponential decay of seismicity after the well was shut in, suggesting that pore pressure diffusion in a critically stressed fractured reservoir is sufficient to explain long-lasting post-injection seismic activity as observed in Basel. We then investigate alternative injection scenarios, using Monte Carlo simulations

to capture the uncertainties in fault locations and stressing conditions. We show that the number of induced events depends not only on the total injected volume but also on the injection strategy. We demonstrate that multi-stage injection schemes are superior to single-stage ones, since the former are associated with less seismic risk and can generate at least the same revenue in the long term.

Key words: Induced Seismicity; Enhanced Geothermal Systems; Numerical Modelling; Probabilistic Forecasting; Discrete Fractures Modelling;

1 INTRODUCTION

In the context of the exploitation of deep geothermal energy, induced earthquakes are both a blessing and a curse. Shearing of existing fracture zones of all scales is a unique tool that permanently alters the permeability of rock volumes, such that fluids can circulate through them more efficiently (Jefferson W. Tester Brian J. Anderson & Jr., 2006; Giardini, 2009), creating a lasting heat exchanger in the deep underground. This is the typical pathway to create so-called Enhanced Geothermal Systems (Evans et al., 2004; Jefferson W. Tester Brian J. Anderson & Jr., 2006), also referred to as Hot Dry Rock and Deep Heat Mining, in the crystalline basement, typically at a depth of $3-5$ kilometres and temperatures upwards of 150°C. This geothermal reservoir stimulation will mobilise existing fractures through the injection of moderate amounts of fluids (typically a few tens of thousands of cubic metres of water) at high overpressures, a process that usually takes several days or weeks to complete (Häring et al., 2008; Evans et al., 2004; Gaucher et al., 2015). Induced micro-earthquakes ($M_L < 2.0$) are also an important tool to monitor and image processes within the evolving reservoir (Häring et al., 2008; Hirschberg et al., 2015) and thus contribute to steering the operations.

Induced seismicity is, however, also a curse and often the biggest obstacle to a successful geothermal project, and a major challenge also for other GeoEnergy applications (Atkinson & Eaton, 2020; Ellsworth, 2013; Grigoli et al., 2017; Lee et al., 2019). In general, induced seismicity can be linked to: both conventional and non-conventional hydrocarbon production, geothermal energy exploitation, mining operations, water impoundment, CO2 sequestration and natural gas storage operations ((Grigoli et al., 2017)). These activities can alter the stress field of the shallow Earth's crust by pore pressure changes, or volume and/or mass changes inducing or triggering seismicity (Ellsworth, 2013). Moreover, they can be a nuisance or even

a danger to the local population, which can strongly undermine the societal acceptance of a project (Trutnevyte & Wiemer, 2017; Grigoli et al., 2018; Hirschberg et al., 2015). In some cases, they even pose a seismic risk too large to accept (Giardini, 2009; Mignan et al., 2015). Examples of projects that have been abandoned due to induced seismicity are the Basel and St. Gallen geothermal projects (Switzerland), the Castor offshore gas storage project (Spain), the Blackpool fracking-related operations (UK), the Pohang geothermal project (South Korea), waste-water injection wells in the US and Canada, and, finally, the Groningen gas field (Netherlands). The combined economic losses associated with the loss of operation due to induced seismicity likely exceeds €30 billion to date. These failed projects highlight the key challenges related to induced seismicity: despite greatly intensified research efforts by many groups over the past decades, the fundamental physical understanding associated with complex chemical-thermal-mechanical interactions and the complex boundary conditions governing induced seismicity are still not sufficiently understood to allow for enough accurate forecasts and mitigation (Yeck et al., 2017; Goebel & Brodsky, 2018; Trutnevyte & Wiemer, 2017; Grigoli et al., 2018; Candela et al., 2018).

EGS technology is widely considered as a highly attractive source of 'green' energy (i.e. low carbon and close to renewable energy). EGS technologies in principle would allow geothermal energy production to be no longer confined to volcanic or hydrothermal regions but to become a valuable resource for many regions. However, induced seismicity related to the stimulation of EGS reservoirs has been a major setback for the development of the technology, since investors need not only to consider the risk of drilling an under-performing well, but also the seismic hazard and its social aspects. The failed Basel EGS project in 2006 highlighted the challenge related to induced seismicity (Giardini, 2009; Häring et al., 2008). Following a widely felt and slightly damaging magnitude Mw 3.2 event and a subsequent risk analysis (Baisch, S., Carbon, D., Dannwolf, U., Delacou, B., Devaux, M., Dunand, F., Jung, R., Koller, M., Martin, C., Sartori, 2009), the project was terminated. A more recent instructive example of the state of the art and current challenges related to EGS projects is the Mw 5.5 Pohang (South Korea) earthquake in November 2017. Grigoli et al. (2018) and Kim et al. (2018) have proposed that the event was likely induced by repeated stimulation activities related to a nearby EGS creation, in a first attempt in Korea to exploit deep geothermal energy. According to an assessment by the Korean Ministry of the Interior and Safety, the earthquake left 1,800 people displaced and 135 injured as well as damaging 57,000 structures that cost around 144.5 billion won (€110 million), making it the most catastrophic induced earthquake related to deep geothermal energy exploitation (Lee et al., 2019). Last but not least, induced

seismicity in EGS context also needs to be considered not only during the stimulation, but also during the operation and post-operational phase of EGS reservoirs (Mignan et al., 2019). However, the example of Soultz-sous-Forrêt shows that limiting induced seismicity is possible, albeit with a negative impact on production (Schill et al., 2017).

To advance EGS technologies and allow for their widespread deployment, we need to develop the ability to optimise the use of induced seismicity as a tool for reservoir stimulation, while also keeping the risk posed by induced earthquakes to an acceptable level. Our study is tackling this highly challenging balancing act in possibly the most quantitative way to date: given a stimulation strategy for the wells of an EGS, our model enables near-real-time applications to forecast induced seismicity as required for Probabilistic Seismic Hazard and Risk Assessments (PSHAs) while simultaneously forecasting the maximum expected electrical power generation, which is useful for Probabilistic Reservoir Performance Assessments (PRPAs). We can then analyse and optimise the trade-off between safety and performance and study optimal reservoir stimulation and operation strategies. Last but not least, our EGS reservoir simulator can be used to study and understand the fundamental processes that govern induced seismicity and reservoir creation.

1.1 Existing approaches to model EGS systems

Induced seismicity models in general, and reservoir models for EGS in particular, can broadly be grouped into three classes (e.g. Gischig & Wiemer (2013); Gaucher et al. (2015); Király-Proag et al. (2016)): statistical, physics-based and hybrid. In general, statistical models for induced seismicity (e.g. Hainzl & Ogata (2005); Bachmann et al. (2011); Mena et al. (2013); Mignan et al. (2017); Broccardo et al. (2017)) are conceptually and computationally simple and include aleatory uncertainty. They are often very robust and perform surprisingly well (Mena et al., 2013; Király-Proag et al., 2016, 2018). However, they do not explicitly account for the complex and interacting geo-mechanical, hydraulic, chemical and physical processes governing induced seismicity (e.g. fluid flow in fractures, permeability changes, and stress interaction) and typically do not allow the economical success of a reservoir stimulation to be assessed. Physics-based models on the other hand (e.g.Olivella et al. (1994); Bruel (2007); Kohl & Mégel (2007); Baisch et al. (2010); Rinaldi et al. (2015); McClure & Horne (2011); Deb & Jenny (2017a,b) do consider underlying physical processes to a variable degree, and are assumed to perform better when operational conditions change substantially, such as for the shut-in period, and for long-term forecasts. However, these models are often difficult to calibrate, carry large uncertainties due to the limited knowledge on faults and relevant

stressing conditions, and carry high computational expense, typically precluding their use in near-real-time applications.

Sharpness is a property of forecasts that indicates how concentrated the predictions from a model are (Gneiting et al., 2007). Although stochastic models can easily be calibrated to return the marginal distribution of induced seismicity observed in EGS (Shapiro & Dinske, 2009; van der Elst et al., 2016), they are rather not sharp since they provide little insight to the mechanisms actually causing induced seismicity and they do not differentiate between scenarios. Forecasts of induced seismicity are expected to be sharper with a deterministic model, but are typically too complex to be effortlessly calibrated (White et al., 2018). This explains why the usage of purely physics based models is limited to testing scenarios (Ucar et al., 2018; Wassing et al., 2014; Riffault et al., 2018) and for inferring induced seismicity sequences (Yoo et al., 2021; Farkas et al., 2021). Similar limitations are apparent when predicting the enhancement of permeability during the creation phase (Pritchett, 2015; AbuAisha et al., 2016), the thermal revenue during the production phase (Llanos et al., 2015; Wang et al., 2019), the overall success of an EGS project over many phases (Li et al., 2019; Liao et al., 2020), and inferring initial thermal conditions (Vallier et al., 2019).

When data from an EGS reservoir are limited, then less sharp but simpler models are preferred for assessments (O'Sullivan & O'Sullivan, 2016; Olasolo et al., 2016). The network of fractures inside an EGS reservoir is an inhomogeneity that has a pivotal role on the spatiotemporal respond of the reservoir to wells' operations. As a result, modeling discrete fractures is one of the desired features from EGS simulatiors (Sanyal et al., 2000). Completely neglecting the effect of fractures when data are limited is not advised. Several methods exist for modeling fractured reservoirs (Lemonnier & Bourbiaux, 2010; O'Sullivan & O'Sullivan, 2016; Berre et al., 2019). The discrete fracture models reproduce the widest range of observed responses in fractured reservoirs (Blessent et al., 2011; Vitel & Souche, 2007; Egya et al., 2019; Berre et al., 2021) thanks to their fidelity to fracture-fracture and fracture-wells intersections.

Hybrid models, also called stochastic models, are a mix between physical models and statistical models, and aim to exploit the benefits of both approaches Gischig & Wiemer (2013); Gischig et al. (2014); Rinaldi & Nespoli (2017); Zbinden et al. (2020); Langenbruch et al. (2018). The goal of hybrid model development is to include some first-order physical processes and replace more complex physical considerations with statistical methods or stochastic processes. In our case, the first-order physical process that we are representing is fluid flow with pore-pressure diffusion inside a fracture network. As discussed in detail in subsequent chapters, hybrid models in essence consider seismicity as a Markovian process, where probable

earthquakes are treated as so-called 'seeds'. The properties of the seeds are sampled with the transition probability of the Markovian process, and the hidden mechanism triggering the seeds is modelled by numerically solving a set of deterministic governing equations.

We believe that a discrete representation of fractures within hybrid reservoir models is a critically important step needed for advancing not only reservoir modelling, but also seismicity and power-generation forecasting, and this is the focus of this study. Fracture networks dominate flow and hence temperature distribution in the reservoir, and they also control the space-time-magnitude evolution of induced seismicity. The highly important but also highly sensitive nature of their effect is illustrated in Fig. 1, where the steady-state pressure diffusion is simulated with the adaptive Hierarchical Fracture Representation (Karvounis & Jenny, 2016) for three fractured rocks that should have identical televiewer logs (i.e. the same fractures interface the two boundary sides) and the minimal differences in their fracture networks would not be detectable before a stimulation. Three fracture networks are depicted in Fig. 1, where the one at the left is from the outcrop in Hornelen, Norway (Bour, 2002), while the middle and the right network differ from it only by one and three small fractures that have been manually added in sensitive areas. Because single fractures can allow for flow into areas that without this fracture would not be activated at all, these minor changes result in a highly non-linear response in quite different pressure distributions, different fault reactivation patterns and different seismicity.

We argue here that in order to understand and model the induced seismicity and the reservoir properties, it is critically important to explicitly consider the discrete fracture networks. Figure 1, however, also illustrates the limitations in deterministically forecasting the stimulation of a reservoir: because any given model will never have the necessary detailed knowledge on fracture distribution and stressing levels at faults, a single model can be substantially wrong. Therefore, we propose here that in order to represent the uncertainties adequately, probabilistic modelling using Monte Carlo simulation is needed and allows us to describe the average expected behaviour of the system, averaged over many possible realisations. We then not only describe the mean behaviour of a reservoir, but can also characterise the uncertainty in this assessment, a critical input when computing probabilistic seismic hazard and risk.

There is one additional implication from the non-linear dependence on the fracture network shown in Fig. 1: because the a-priori uncertainties before a stimulation are inherently large and cannot be substantially reduced by geological or geophysical characterisation (e.g. (Broccardo et al., 2020)), seismicity and reservoir forecasting models must be re-calibrated on the fly as new data emerges. We have developed our stochastic discrete fracture model presented here

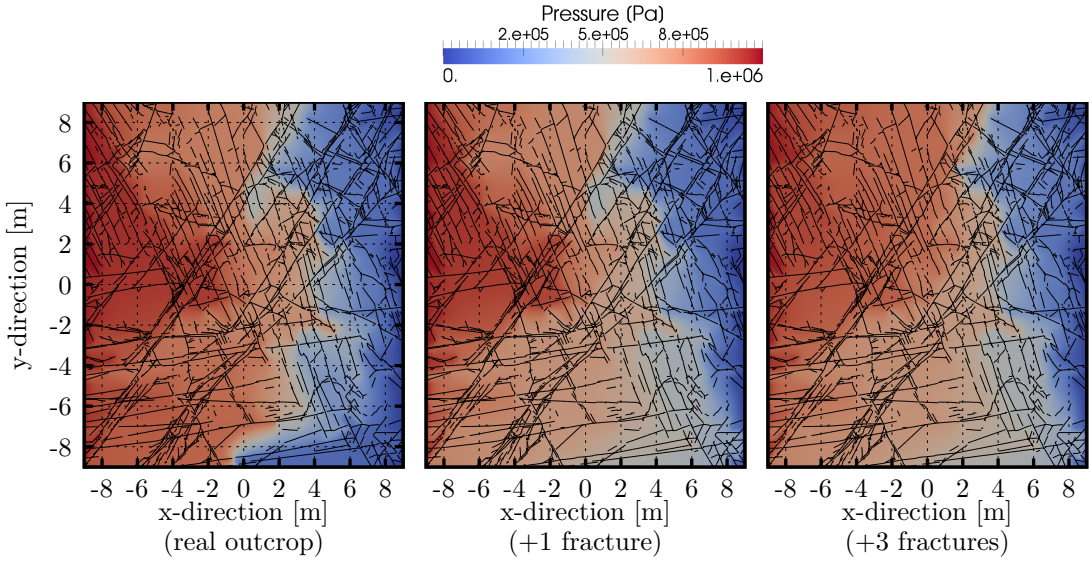

Figure 1. Steady state pressure diffusion is simulated with HFR-Sim (Karvounis & Jenny, 2016) for three fracture networks, where a 1 MPa pressure difference is applied at their side boundaries. Although the networks look identical as they differ by only a few tiny fractures, in practice they would return very different observations due to their large differences in connectivity. A discrete fracture model can efficiently simulate such scenarios.

with this need in mind, such that it can be readily used within so called 'Advanced Traffic Light Systems' (ATLSs) that automatically and dynamically adapt the seismicity forecast as new data during a stimulation are collected (Mignan et al., 2017; Grigoli et al., 2017).

2 GOVERNING EQUATIONS FOR THE DISCRETE FRACTURE HYBRID MODEL (DFHM) AND FORECASTS WITH IT

We consider here the two most important phases in the lifetime of an EGS power plant when decisions on induced seismicity and reservoir development strategies need to be taken. These two phases are the reservoir stimulation phase, where the permeability of the EGS reservoir is artificially enhanced, and the operation phase, where the heat stored inside the reservoir is extracted and converted into electrical energy. Activities during the stimulation phase of course influence the operational phase.

In this section, we introduce a hybrid reservoir and induced seismicity modelling approach. What is new about this is that it combines embedded discrete fracture modelling for modelling flow and heat transport with stochastic modelling of induced seismicity. We then apply the model to investigate the effectiveness of different reservoir stimulation and operation

strategies. Our model will allow us to simultaneously optimise seismic safety and reservoir performance (in terms of heat revenues) of the future EGS.

A three-dimensional (3D) EGS domain $\Omega \in \mathbb{R}^3$ is considered that consists of a low-porosity and low-permeability hot porous medium (e.g. granite), which is fractured. The stimulation and production strategy $q(t)$ is the rate of fluid volume at each moment t that either has been injected ($t \leq t_0$) or will be injected ($t > t_0$), where t_0 is always the present moment. It is arbitrarily decided that $q > 0$ for injections. We assume the future flow rate $q(t)$ to be the only parameter controlled by the operators of the EGS.

Below, scalar variables are written with standard type, vectors in bold type, and tensors in upper-case bold type with an accent, while random variables are given with a bar above them. For example, $\hat{\mathbf{K}}(\mathbf{x}, t)$ is the permeability tensor at the point $\mathbf{x} \in \Omega$ and for time t, and $\bar{M}_w$ is the moment magnitude of an induced event. Probabilities are denoted with $\mathbb{P}$, probability density functions (PDF) with $\mathfrak{f}$, and cumulative density functions (CDF) with $\mathbf{F}$. For example, if $\mathbb{P}\left(\bar{M}_w \geq M_w\right)$ is the probability of a randomly drawn $\bar{M}_w$ being greater or equal than a value M_w, the CDF of $\bar{M}_w$ is

$$\mathbb{F}_{\bar{M}_w} = \mathbb{F}\left(M_w\right) = 1 - \mathbb{P}\left(\bar{M}_w > M_w\right) \approx 1 - 10^{-b(M_w - M_{w_{min}})}, \tag{1}$$

and the PDF of M_w is

$$\mathfrak{f}_{\bar{M}_w} = \mathfrak{f}\left(M_w\right) = \mathbb{P}\left(\|\bar{M}_w - M_w\| < dM_w\right) = \frac{d\mathbb{F}_{\bar{M}_w}}{dM_w}, \tag{2}$$

To represent the frequency-size distribution of earthquakes, we use a power law distribution commonly referred to as the Gutenberg-Richter distribution (Gutenberg & Richter, 2010), $\log_{10}(N) = a - bM_w$, where b is a constant representing the relative size distribution and a the activity rate. The rate can be truncated by expert choice at an upper bound, the maximum magnitude $Mmax$. Finally, sequences of discrete values are written in braces where the subscript denotes the index of the first value in this sequence and the superscript denotes the index of the last one. For example, a sequence that includes the moment magnitudes from the n-th to the m-th event can be written as $\{M_w\}_n^m = \{M_{w_n}, M_{w_{n+1}}, \ldots, M_{w_m}\}$. Also, it holds that $\{X, Y\}_n^m = \{\{X\}_n^m, \{Y\}_n^m\}$ and $\{X\}_1^m = \{X\}^m = \{X_1, X_2, \ldots, X_m\}$ for any two sequences X and Y.

2.1 Conservation of mass and energy

The conservation of mass and energy for the single-phase fluid inside the fractures of a reservoir Ω, and the conservation of energy for the solid rock inside Ω can be expressed as

$$\frac{\partial}{\partial t}(\rho\phi) + \nabla \cdot \rho \overbrace{\left(-\frac{\hat{\mathbf{K}}}{\mu}(\nabla p - \rho \mathbf{g})\right)}^{\mathbf{u}} = \rho(q + q^f), \tag{3}$$

$$\frac{\partial}{\partial t}(\phi\rho h) + \nabla \cdot (\rho h \mathbf{u}) = \dot{w}^q + \dot{w}^f + \dot{w}^r, \tag{4}$$

and

$$\frac{\partial}{\partial t}((1-\phi)\rho^r h^r) + \nabla \cdot \left(-\hat{\mathbf{\Lambda}} \cdot \nabla T^r\right) = \dot{w}^s - \dot{w}^r, \tag{5}$$

respectively, where ϕ is porosity, $\hat{\mathbf{K}}$ is the permeability tensor, ρ and μ the density and viscosity of the fluid, $\mathbf{u}$ the Darcy's velocity, $\mathbf{g}$ the gravitational vector, q^f the volumetric source/sink flux of the incompressible fluid away from the bottom of the casing shoes, h and h^r the specific enthalpy of the fluid and the solid phase, respectively, ρ_r and T^r the density and the temperature of the solid medium, $\dot{w}^r$ the rate of heat transported from the solid to the fluid's phase, $\dot{w}^q$ is the heat exchange rate through the wells, $\dot{w}^f$ other heat sources, $\dot{w}^s$ is the rate of other heat source terms inside Ω, and $\hat{\mathbf{\Lambda}}$ is the heat conductivity. The heat exchange between the fluid and the solid phase is proportional to the temperature difference between them; i.e. $\dot{w}^r = C(T^r - T)$, where C is a heat exchange coefficient. Heat conduction inside the fluid filling the fractures is neglected.

The total thermal energy E_{th} recovered from the solid phase and over a period of time t_l is

$$E_{th} = -\int_0^{t_l} \int_\Omega \dot{w}^q dV dt. \tag{6}$$

Only a portion of the extracted E_{th} can be converted into electrical energy E_e. The efficiency η, which is the ratio of electrical power generated by the EGS power plant over the extracted thermal power from the reservoir, depends on the temperature of the produced water T_{out} and hence the total electrical energy produced over a period t_l is

$$E_e = -\int_0^{t_l} \eta \int_\Omega \dot{w}^q dV dt. \tag{7}$$

The pair of modelling parameters $\hat{\mathbf{K}}$ and ϕ are simply called hydraulic properties below, and their enhancement is one of the goals of a stimulation. Ideally, the final permeability inside Ω is high enough to produce E_e at commercially interesting rates and not be too

inhomogeneous, which would promote the development of preferential flow paths that limit the overall E_e.

2.2 Simplifications and discrete fracture modelling

For simplicity, all the material properties ρ, μ, ρ_r and $\hat{\mathbf{\Lambda}}$ are considered constants, and gravitational effects are neglected. EGS reservoirs are characterised by highly inhomogeneous hydraulic properties and by highly anisotropic $\bar{\mathbf{K}}$ due to fractures, which usually have a dominant effect for flow. Aligned to other approaches for the modelling of EGS during stimulation, a linear relationship between ϕ and p is considered, and mass conservation is modelled by a diffusion process for p. In particular, when seismicity does not occur and p is continuous, then eq. (3) results in the linear diffusion

$$S\frac{\partial}{\partial t}(p) + \nabla \cdot \overbrace{\left(-\frac{\hat{\mathbf{K}}}{\mu}\nabla p\right)}^{\mathbf{u}} = q + q^f, \tag{8}$$

where S is storativity.

Domain Ω is decomposed into two subdomains Ω^d and Ω^f, in a way that allows the adaptive Hierarchical Fracture Representation (a-HFR) modelling approach to be employed (Karvounis & Jenny, 2016). The set Ω^f consists of N_f important fractures that are going to be treated discretely and $\Omega^f = \Omega^f_1 \cup \cdots \cup \Omega^f_{N_f}$, where Ω^f_i is the i-th discrete fracture. The set Ω^d, which in a-HFR is simply called the "damaged matrix", is the rest of Ω. Here, Ω^d is three-dimensional, and it surrounds the two-dimensional manifolds for the N_f discrete fractures of Ω^f. Porosity is modelled as

$$\phi \approx \begin{cases} \phi^d_0 + \ddot{\rho}_f \alpha (p - p_0), & \forall \mathbf{x} \in \Omega^d \\ \\ 1 + \alpha(p - p_0)/b^f_i & \forall \mathbf{x} \in \Omega^f_i, \end{cases} \tag{9}$$

where $\ddot{\rho}_f$ is the fracture density inside Ω^d and is defined as the total fracture surface area per unit of volume, α is a compressibility constant for fractures, ϕ^d_0 is the porosity of the damaged matrix when $p = p_0$, and b^f_i is the mechanical aperture of the i-th discrete fracture. Storativity in eq. (8) then equals $S = d\phi/dp$.

For directions along Ω^f permeability k^f is considered isotropic and significantly larger than the isotropic permeability k^d of the damaged matrix Ω^d. The limit scenario, where fractures are smooth parallel plates distanced by b^f_i, is less frequently observed and expected in the reservoirs of EGS. Thus, k^f is not a function of b^f_i here, and it is at most its theoretical maximum $k^f \leq (b^f_i)^2/12$.

Effective permeability in Ω^d is sensitive to the inter-connectivity of its underlying network of fractures, as shown in Fig. (1) and upscaling diffusivity is not a straightforward task. Here and since Ω^d consists only of less important fractures, the detailed geometry of the underlying fractures is neglected. Underlying fractures are assumed to be interconnected enough for k^d to be higher than the permeability of the solid medium. Significantly higher k^d are expected only when an interconnected subset of underlying fractures exists that only consists of fractures with high permeability. The percolation threshold defines when interconnectivity is the most likely scenario and such thresholds are going to be considered later. For example, the percolation threshold for randomly positioned discs that follow a power law size distribution and can have any orientation, increases with increasing density

$$\rho_3^{'} = \pi^2 \dot{\rho} \langle R^3 \rangle, \tag{10}$$

where $\dot{\rho}$ is the number of discs per unit of volume and $\langle R^3 \rangle$ is the third statistical moment of the radii R of the discs (Mourzenko et al., 2005).

2.3 Sampling induced seismicity and its effect on permeability

Hydroshearing due to increased pressure is considered to be the main mechanism of induced seismicity in EGS and is here considered to be the only mechanism for increasing permeability. Whenever the two planes of a fracture slip relatively to each other and over a segment of the fracture Ω_s, then both the mechanical aperture b^f and the permeability k^f increase at the ruptured surface Ω_s. In general, these increases happen only along the ruptured surface Ω_s and are irreversible. For the size $|\Omega_s|$ and its M_w, it holds that

$$\log_{10}(M_0) = \log_{10}(G|\Omega_s||\mathbf{d}_s|) \approx 1.5(M_w + 6.03), \tag{11}$$

where M_0 is the seismic moment, G is the shear module, and $\mathbf{d}_s$ is the mean slip parallel to the Ω_s (Kanamori, 1977). According to the Mohr-Coulomb failure criterion, a hydroshearing event with hypocentre $\mathbf{x}_s$ and source time t_s happens when

$$p(\mathbf{x}_s, t_s) = p_f = \frac{C_0 - \tau}{\mu_s} + \sigma_n, \tag{12}$$

where p_f is the failure pressure of the fracture, μ_s and C_0 the friction and the cohesion of the fracture, and σ_n and τ the normal and shear stresses at $\mathbf{x}_s$, which depend on the Cauchy stress tensor and the unit pole vector of the fracture $\mathbf{n}$ that is normal to Ω_s. For simplicity, the right-hand side of the failure criterion is considered steady in time and p_f is a function of only $\mathbf{x}$, but in general this right-hand side can change both with pressure (e.g. poro-elastic effects) and with time (e.g. stress transfer). Such mechanisms are not considered here.

In our model, induced seismicity, fluid flow and pressure propagation are strongly coupled: shearing on existing fractures (i.e. earthquakes) modulates flow, which in turn may induce future shearing events.

The considerable uncertainty in forecasting induced seismicity is a result of the fact that the density and shape of the existing fracture network is not known in any detail away from the borehole, nor is the stress distribution on these fractures. To address and model these inherent uncertainties, we employ a stochastic modelling approach initially proposed by Gischig & Wiemer (2013) and Goertz-Allmann & Wiemer (2013). Our approach captures the overall statistical distribution of faults but also captures the randomness in the occurrence time, magnitude and location of each individual event.

We exploit as input the observation that M_w from past EGS stimulations follows a Gutenberg-Richter-like distribution consistent with eq. (1). Traditionally, the b-value in eq.(1) is calibrated and then the probability of any sequence of $\{M_w\}^m$ can be approximated, where the size of the expected sequence N_{eq} is also associated with a certain probability conditioned on the planned injection q. Here, $\bar{M}_w$ are also expected to be sampled with a calibrated form of eq. (1), but this time a more detailed catalogue $\{\bar{\mathbf{\Theta}}\}^{N_{eq}} = \{M_w, \mathbf{x}_s, t_s, \Omega_s, b^f, k^f\}^{N_{eq}}$ is sampled and the size N_{eq} is restricted by the deterministic solution of eq. (3) and the sampled hydraulic changes $\{b^f, k^f\}^{N_{eq}}$.

With a view to simplifying the PDF with the elements of the catalogue that are sampled, the following simplifications are considered: i) $\bar{M}_w$, $\bar{b}^f$ and $\bar{k}^f$ are independent of all random properties, and $\bar{M}_w$ is sampled as in eq.(1), ii) $\bar{\mathbf{x}}_s \in \bar{\Omega}_s$, and the size of $\bar{\Omega}_s$ depends only on the sampled $\bar{M}_w$. Overall, the PDF for sampling the catalogues here is simplified to

$$\begin{aligned} \mathfrak{f}_{\bar{\mathbf{\Theta}}} &= \mathfrak{f}(M_w, \mathbf{x}_s, t_s, \Omega_s, b^f, k^f | q) \\ &\approx \mathfrak{f}(t_s|\mathbf{x}_s, \Omega_s, q) \cdot \mathfrak{f}(\mathbf{x}_s, \Omega_s|M_w) \cdot \mathfrak{f}(b^f, k^f) \cdot \mathfrak{f}_{\bar{M}_w}, \end{aligned} \tag{13}$$

where only the source time t_s depends on q and due to the criterion (12) the probability of an event existing with $\bar{t}_s$, given q, and the orientation of Ω_s is

$$\mathfrak{f}(t_s|\mathbf{x}_s, \Omega_s, q)dt \approx \int_0^\infty \delta(p(\mathbf{x_s}, t) - p_f) \cdot \mathfrak{f}(p_f|\mathbf{x}_s, \Omega_s)dp_f, \tag{14}$$

where dt is an infinite small time period around t_s, δ is the Dirac delta function that is non-negative only when the solution of eq. (3) p equals p_f, which is treated as a random property with its own PDF $\mathfrak{f}(p_f)$.

Although past hybrid models never formalised their stochastic part as is done here, all hybrid models are Markovian processes with a transitional PDF $\mathfrak{f}_{\bar{\mathbf{\Theta}}}$ that is simplified by considering conditional independencies as in eq. (13). Once all PDFs are calibrated and trained

on the basis of collected observations, then it is possible to sample seismicity by simply forecasting the hidden mechanism p. Different hybrid models can use similarly calibrated PDFs. Thus, their differences and their performance depend on their forecasts for p. Discrete fracture modelling can offer accurate and precise modelling of breakthrough times and of the next source time t_s of a synthetic catalogue. Here, focus is not on calibrating the PDFs, but on exploiting the accurate and precise predictions of breakthrough times for p that discrete fracture models, as can be provided by a-HFR.

2.3.1 Optimising EGS development

During reservoir stimulation, EGS developers need to balance seismic safety considerations and the economical viability of the project. Important decisions on the stimulation strategy need to be taken not only in the planning phase but also in near-real time and despite considerable uncertainty. One of our goals is to provide operators with real-time decision support. The requirements of the operator can be quantified by a utility function $\mathcal{U}(\mathbf{f}, q)$, where $\mathbf{f}$ is a vector of uncertain variables that are not yet observed.

To enable decision support, our embedded discrete fracture hybrid model (DFHM) combines the deterministic modelling as described in subsection 2.2 and the stochastic modelling as in subsection 2.3. A forward simulation with this DFHM and for a given q returns samples of equally probable $\mathbf{f^k} = \{\{\Theta\}^{N_{eq}}, E_e^{max}\}^k$, and most important properties for our optimisation are

(i) N_{eq} is the total number of induced earthquakes;

(ii) the maximum expected M_w; and

(iii) E_e^{max} the electrical generation for the forecasted hydraulic properties of $\{\Theta\}^{N_{eq}}$ and for the circulation rate that maximises E_e.

A Bayesian approach is followed for predicting the utility functions given $q(t)$

$$U(q) = \langle \mathcal{U}(q) \rangle \approx \lim_{M \to \infty} \frac{1}{M} \sum_{k=1}^{M} \mathcal{U}(\mathbf{f^k}, q), \tag{15}$$

where M is the sample size of independent forecasts, $\mathbf{f^k}$ is the k-th forecast returned by DFHM, and the approximation above is actually a Monte Carlo (MC) integration. The approximated U is associated with a statistical error $\pm\delta U$ that depends on the variance and which equals

$$\delta U = \frac{1}{M} \sqrt{\sum_{k=1}^{M} \mathcal{U}^2(\mathbf{f}^k, q) - MU^2}. \tag{16}$$

We can now search for the $q(t)$ that maximises their respective utility function. For any

two stimulation strategies it is assumed that q_1 is more preferable than q_2, if and only if $U(q_1) \geq U(q_2) + \delta U(q_2) + \delta U(q_1)$. This way, comparison between different q can be performed before the two MC integrations reach the same accuracy, and for $M \gg 1$.

Note that during the production phase, any line search method can return the optimum rate that maximises E_e^{max}. Here, the Brent algorithm, offered by the GSL library, has been employed (Gough, 2009).

3 IMPLEMENTATION AND ACCELERATION OF DFHM

We will now describe the implementation of DFHM in some detail. The overall framework is implemented as a C++ code. The EGS simulator HFR-Sim solves eqs. (3)-(5) with the a-HFR approach, and it can estimate the evolution of pressure and temperature for a given fracture network, which evolution is necessary for E_{th} and E_{el}. The implemented stochastic seismicity model (referred to below as the 'seed' model) considers completely 3D disc-shaped discrete ruptures, and it is sequentially coupled with the flow solvers of HFR-Sim. To accelerate the calculations, a variation of the Adaptive Implicit Method (AIM) has been implemented in HFR-Sim.

As explained in section 2, the goal of DFHM is to approximate expected utility functions that depend on both E_{el}^{max} and M_w^{max} by simulating M different scenarios. At each time step with step size Δt that HFR-Sim solves for p in eq. (3), then the seed model samples an arbitrary number of induced seismicity events, and finally the hydraulic properties of the a-HFR model are updated according to the sampled seismicity. The final a-HFR model, which superimposes on the initial permeability field the enhanced permeability of the N_{eq} sampled hydrosheared fractures, is then employed for finding the circulation rate that maximises electricity and the amount of this maximum electricity E_{el}^{max}.

3.1 Deterministic modelling

The EGS simulator HFR-Sim employs the adaptive hierarchical fracture representation (a-HFR), specially designed for dynamically changing fracture networks (Karvounis & Jenny, 2016). Here, the main characteristics are briefly described. The details of the simulator can be found in the literature (Karvounis & Jenny, 2016; Karvounis, 2013).

In HFR-Sim, the damaged matrix and the solid rock continuum are discretised with two identical 3D structured meshes, and discrete fractures are treated as 2D manifolds meshed with a 2D structured mesh embedded in the 3D cells of both the damaged matrix and the

solid rock continuum. The final mesh is the combination of all these structured meshes and consists of N cells filled with fluid (fractures and damaged matrix) and N_r cells for the solid rock. Ω_i is the subdomain of the i-th damaged matrix cell and Ω_k^r is the subdomain of the k-th rock volume.

Mass and heat transport inside Ω are modelled by implementing the finite volume method for each cell of the mesh. For each cell i filled with fluid, the mean values of pressure $P_i = \langle p \rangle$ and temperature $T_i = \langle T \rangle$ inside the cell are approximated. For each cell k of the solid rock, only its mean temperature is approximated as $T_{r,k} = \langle T^r \rangle$, and a linear relationship between temperature and enthalpy is considered. Mass exchange and heat transfer due to advection are possible only between the N cells. Heat transfer due to conduction is possible between all pairs of $N + N_r$ cells that share a boundary.

The superscript n (when applicable) denotes the time step to which this value corresponds. For example, P_i^n is the mean pressure inside the i-th cell and by the end of the n-th time step.

3.1.1 Numerical modelling of flow and heat transport with HFR-Sim

The discretised forms of eqs.(3)-(5) in HFR-Sim are: for incompressible mass conservation in the N degrees of freedom (dofs)

$$\begin{aligned} \frac{V_i^{n+1} - V_i^n}{\Delta t} &= \sum_j^N \overbrace{C_{ij}^n \left(P_j^{n+1} - P_i^{n+1} \right)}^{F_{ij}^{n+1}} \\ &+ Q_i^{n+1}, \end{aligned} \tag{17}$$

for heat advection inside the fluid in the N dofs

$$\begin{aligned} V_i \frac{T_i^{n+1} - T_i^n}{\Delta t} &= -\sum_j^N F_{ij} \overrightarrow{T_{ij}}^{n+1} \\ &+ \frac{1}{c_h \rho} \sum_k^{N_r} C_{r,ki} (T_{r,k}^{n+1} - T_i^{n+1}) \\ &+ \frac{W_i^{n+1}}{c_h \rho}, \end{aligned} \tag{18}$$

and for heat conduction inside the solid continuum in the N_r dofs

$$\begin{aligned} V_{r,k}\rho^r c_h^r \frac{T_{r,k}^{n+1} - {T_{r,k}}^n}{\Delta t} &= \sum_{l}^{N_r} K_{kl}(T_{r,l}^{n+1} - T_{r,k}^{n+1}) \\ &- \sum_{i}^{N} C_{r,ki}(T_{r,k}^{n+1} - T_i^{n+1}) \\ &+ W_{r,k}^{n+1}, \end{aligned} \tag{19}$$

where V_i and $V_{r,k}$ respectively are the total volume of fluid and of rock inside the corresponding cells, C_{ij} and F_{ij} are the transmissibility between and the volumetric flow rate between two fluid cells, K_{kj} is the constant coefficient for heat flux due to conduction between rock cells k and j, $\overrightarrow{T_{ij}}$ represents the upwind scheme for temperature, where

$$\overrightarrow{T_{ij}} = \begin{cases} T_i, & \text{if } F_{ij} \geq 0 \\ T_j, & \text{otherwise} \end{cases}, \tag{20}$$

boundary conditions from the governing eqs. are captured by Q_i, W_i and $W_{r,k}$, and finally $C_{r,ki}$ is a heat coefficient for heat flux due to conduction between the solid and the fluid continua. Note that the mesh generator of HFR-Sim calculates the values not only of C_{ij} and K_{kj}, but also of $C_{r,ki}$ for the given geometry and material's properties (Karvounis, 2013). However, HFR-Sim does not assume upscaling techniques for the permeability of the damaged matrix or for the efficiency with which the damaged matrix exchanges heat with the solid. Users are expected to provide the necessary input.

Based on the above, the DFHM employs HFR-Sim and solves implicitly for the N values of P_i^{n+1} in (17). Changes in the mean fluid volume are modelled as

$$V_i^{n+1} - V_i^n = \overbrace{V_{i,0}^{n+1} - V_{i,0}^n}^{\Delta V_0} + |\Omega_i| S_i (P_i^{n+1} - P_i^n), \tag{21}$$

where $|\Omega_i|$ is the size of the cell, S_i is its storativity, and $\Delta V_0 \neq 0$ when new void volume is created in or along Ω_i due to seismicity at the n-th time step. When the i-th cell corresponds to a newly added discrete fracture and P_i^n is not initialised, then the value of P_i^n is interpolated from the surrounding pressure values, and it is then corrected for the seismic pumping pressure drop, which is user-defined. The set of N linear equations that is derived by combining eqs. (17) and (21) is numerically solved with an iterative algebraic multigrid method (AMG) from the Trilinos package (Heroux et al., 2005) and the implicit solution p is approximated.

During the production phase, the DFHM considers the steady-state solution of (17), which is again solved with an AMG solver, and employs the steady-state volumetric flux F_{ij} for modelling heat advection. Heat exchange between the damaged matrix and the solid rock

cells is modelled as

$$\dot{w}^r = \frac{60}{(1/\ddot{\rho}_f)^2}|\hat{\mathbf{\Lambda}}|(T^r - T), \tag{22}$$

which is a source term similar to how mass transfer is modelled by a 3D dual-rate model. Here, where the two cells are going to be identical, coefficient $C_{r,ki}$ equals the product of $(60\ddot{\rho}_f^2|\hat{\mathbf{\Lambda}}|)$ with $|\Omega_i|$. Then and for each time step, HFR-Sim combines (18) and (19) into one linear system of $N + N_r$ equations and implicitly solves both for T_i^{n+1} and $T_{r_k}^{n+1}$. HFR-Sim solves the set of $N + N_r$ linear equations from eqs. (18)-(20) with a KLU direct solver also from the Trilinos package Heroux et al. (2005).

3.1.2 Adaptive implicit solutions for overpressure

In principle, the computational cost of an AMG linear system solver increases linearly with the number of dofs, and hence the overall cost for a DFHM Monte Carlo integration should increase linearly not only with the number of simulated scenarios, but also with the size of the linear system that the AMG needs to solve and with the average number of necessary time iterations. Still, the dense computations required even by a fast solver like AMG can be an important bottleneck.

A significant reduction in the number of time iterations is easily achieved with the adaptive step size method, where the time step Δt increases by a certain factor Δt_B when diffusion is linear. Here, Δt increases when there is a lack of considerable seismicity and the boundary conditions do not change. If this is not the case, then Δt resets to a small value Δt_0. Eventually, fewer time iterations are required for periods with low rates of seismicity.

A variation of the Adaptive Implicit Method (AIM) (Thomas & Thurnau, 1983; Russell, 1989) is employed for reducing the number of unknowns that need to be solved with the AMG. In the traditional AIM, a subset of dofs is treated implicitly and the rest of them are treated explicitly. There, a $(2g + 1)^3$-stencil is employed for the discretised diffusion equation, where $g \geq 1$ (e.g. 27-stencil for $g = 1$). The explicit solution of each cell for the next time iteration is a linear combination of its neighbouring $((2g + 1)^3 - 1)$ solution, and after m time iterations it is the linear combination of its $(1 + 2gm)^3 - 1$ neighbouring solutions. The weighting of each neighbouring solution is such that it defines the accuracy of the explicit solution, and a maximum time step Δt_{CFL} exists up to which a stencil can return stable explicit solutions.

Here, the parabolic nature of the diffusion process is exploited, where cells that are expected to be virtually unaffected by the diffusion process are not solved at all, i.e. neither implicitly nor explicitly. To this end, pre-processing is required before each time step. Users

choose a very low value for the diffusing property δp_{min}, and as before, a 'stencil' is considered and its Δt_{CFL} is found for each cell.

Damaged matrix cells are separated into three subsets $\mathcal{A}$, $\mathcal{B}$ and $\mathcal{C}$, where set $\mathcal{C}$ is made up of the cells to be omitted from this iteration's calculations. Cells belonging to discrete fractures or wells, always belong in $\mathcal{A}$. Also part of $\mathcal{A}$ are the cells penetrated by a fracture or a well, as well as the cells with mean pressure that has been greater or equal to $(\delta p_{min} + p(t < 0))$ during the simulation. Classification of the remaining damaged matrix cells in $\mathcal{B}$ or in $\mathcal{C}$ is based on the relation of Δt to the CFL condition and the size of the stencil. The ratio $\Delta t / \Delta t_{CFL}$ shows how many more time iterations are required for modelling diffusion explicitly, and n^* is the total number of such iterations for the i-th cell. Set $\mathcal{B}$ consists of all the cells whose stencil after n^* iterations does not include a cell from $\mathcal{A}$. Set $\mathcal{C}$ consists of the remaining damaged matrix cells. No flux condition is assumed along the boundaries of $\mathcal{B}$ with $\mathcal{C}$, unless the boundaries of Ω are reached by $\mathcal{B}$.

The domain decomposition described above can be efficiently implemented for the equidistant structured meshes of the DFHM. From all cells that are newly added in $\mathcal{A}$, a graph search is initiated and it estimates for all non-$\mathcal{A}$ cells the maximum number of explicit iterations m_i, for which their stencil $(1 + 2gm_i)^3$ does not require set $\mathcal{A}$. Considering the typical indexing (i_1, i_2, i_3) for structured meshes, where integer i_k is the position of the cell at the k-th direction, then m_i can be quickly found:

$$gm_i = \min_{\forall (j_1, j_2, j_3) \in \mathcal{A}} \left(\min_{k=1,2,3} (|i_k - j_k|) \right). \tag{23}$$

Eventually, the set $\mathcal{B}$ consists of all cells with $m_i \leq n^*$ and m_i needs to be updated only when the set $\mathcal{A}$ changes.

3.2 Stochastic modelling

The stochastic modelling of induced seismicity is the element of the DFHM that generates the input for the deterministic modelling. As in previous hybrid models (Gischig et al., 2014; Karvounis et al., 2014; Rinaldi & Nespoli, 2017), the 'Seed model' approach is employed, which allows hybrid models to be operated as Markovian processes with a Bayesian network for their transitional probability. For each hybrid simulation a set of seeds is sampled, where each seed represents a potential hypocentre of an induced earthquake rupturing a discrete fracture. Subsection 3.2.1 describes how an initial set of seeds is sampled at the beginning of each simulation. How induced seismicity is modelled given an HFR-Sim solution P_i^n is explained in

3.2.2, and finally how the hydraulic properties for the HFR-Sim simulation change thereafter is presented in 3.2.3.

3.2.1 Initiation of a set of seeds

In line with other hybrid models, the implemented DFHM requires as its input the domain $\Omega_{seed} \supset \Omega$, inside which seeds with density $\dot{\rho}_s$ are to be sampled, the b-value of the Gutenberg-Richter law, a pair of friction μ and cohesion C_0 that are fixed, a scalar $\sigma^2 \geq 0$, the range $[M_{w_{min}}, M_{w_{max}})$ from which moment magnitudes are to be sampled, and finally, the direction and stress magnitude of the principal stresses. For the sake of simplicity, three orthogonal vectors are defined that are parallel to the principal stress direction and their length is equal to the respective average principal stress $\langle \boldsymbol{\sigma_1} \rangle$, $\langle \boldsymbol{\sigma_2} \rangle$ and $\langle \boldsymbol{\sigma_3} \rangle$.

Based on the above input and by using a random number generator, the DFHM samples the following properties per seed:

(i) a hypocentre $\bar{\mathbf{x}} \in \Omega_{seed}$ that follows a uniform distribution in Ω_{seed} according to $\dot{\rho}_s$;

(ii) a unit vector $\bar{\mathbf{n}}$ that is normal to the ruptured surface, it points upwards and follows a uniform distribution in a subset of $[0, 2\pi]$, which vector is going to be the pole of the discrete fracture that will be added to the model only when the seed has a large ruptured surface and is triggered by excessive pressure;

(iii) a moment magnitude

$$\bar{M_w} = M_{w_{min}} - (M_{w_{max}} - M_{w_{min}}) \frac{log_{10}(\bar{m}_w)}{b}, \tag{24}$$

which $\bar{M_w}$ follows the distribution of eq. (1), and it is estimated by sampling a random number $\bar{m}_w \in [0, 1)$ from a uniform distribution; and

(iv) three principal stresses $\bar{\sigma_1}$, $\bar{\sigma_2}$ and $\bar{\sigma_3}$, where each principal stress follows a normal distribution around the size of its average value $|\langle \sigma_k \rangle|$ and a standard deviation equal to the product of σ^2 and this mean size. The principal directions are fixed and parallel to the orthogonal vectors $\langle \boldsymbol{\sigma_1} \rangle$, $\langle \boldsymbol{\sigma_2} \rangle$ and $\langle \boldsymbol{\sigma_3} \rangle$.

Finally and using the above sampled properties, one can estimate a traction vector $\bar{\mathbf{t}}$ and from it a failure pressure $\bar{p}_f$ for each seed, where

$$\bar{\mathbf{t}} = \sum_{k=1}^{3} \frac{(\bar{\boldsymbol{\sigma}}_{\boldsymbol{k}} \bar{\mathbf{n}})}{|\langle \boldsymbol{\sigma_k} \rangle|} \langle \boldsymbol{\sigma_k} \rangle,$$

and $\bar{p}_f$ can be estimated from eq. (12) from the sampled properties, where $\bar{\sigma}_n = |(\bar{\mathbf{t}} \bar{\mathbf{n}}) \bar{\mathbf{n}}|$ and $\bar{\tau} = |\bar{\mathbf{t}} - \bar{\sigma}_n \bar{\mathbf{n}}|$. Similarly to past implementations, a new traction vector is sampled for all

seeds and until a meaningfully large positive $\bar{p}_f$ is sampled. A necessary criterion for ending the resampling of traction for a seed is that the seed does not satisfy the failure criterion of eq.(12) for a friction incremented by a small value $\delta\mu$ defined by the user. An important differentiation of this seed model from the past models is that seeds are allowed to be sampled in sets. Each set can have a different mean orientation, similar to how natural fractures are observed, and a different maximum angle, where only seeds within this angle deviation from the mean orientation are sampled.

In the DFHM, the Box-Muller algorithm is implemented to obtain one normally distributed random value from one uniformly distributed random number (Box & Muller, 1958). A different sequence of pseudo-random numbers is used for each DFHM simulation, and at least nine such random numbers are required per seed, i.e. three for $\bar{\mathbf{x}}$, two for $\bar{\mathbf{n}}$, one for $\bar{m}_w$, and three for the three normally distributed principal stresses. Note, however, that all possible pseudo-random numbers are still discrete values with an equal spacing between them. This results in discrete values of M_w, which however are not equally spaced. Especially when the range of interest $[M_{w_{min}}, M_{w_{max}})$ is large or the b-value small, then this can lead to a small sample space of large discrete values for M_w. Here, this issue is treated by sampling a sequence of uniformly random numbers, until a number is drawn that is less than $1-\epsilon$, where ϵ is a low enough number. Each time the stopping criterion is not satisfied, then the M_w that corresponds to ϵ is temporarily considered as the new $M_{w_{min}}$. The final $\bar{M}_w$ equals the summation of all temporary $M_{w_{min}}$ and the last sampled $\bar{M}_w$. No correlation between $\dot{\rho}_s$ and the fracture density $\ddot{\rho}_f$ is considered here. Of course, both friction and cohesion can be considered random and not fixed, and spatial variations of $\dot{\rho}_s$, $\ddot{\rho}_f$ and of the average pole vector could be correlated and in line with field observations.

The value of $\ddot{\rho}_f$ is usually representative only of the observable area around the drilled rock, and therefore here it is not considered an acceptable indicator of $\dot{\rho}_s$. Aside from all this and as depicted in Fig. 1, discrete fracture simulations can be very sensitive even to tiny local variations of $\ddot{\rho}_f$, and the hybrid model here does not consider repeating events.

3.2.2 Updating the synthetic catalogue of induced seismicity

Every time the set of eqs. (17) is solved, a solution vector $\mathbf{P}^{n+1}$ is obtained, where the i-th element of this vector is an approximation of the mean pressure p inside Ω_i. In the DFHM, this solution $\mathbf{P}^{n+1}$ is employed for approximating p at the hypocentres of the seeds. For each seed, the cell of the damaged matrix Ω_i is found, inside which cell the hypocentre of the seed lies, and the pressure at this hypocentre is considered equal to P_i^{n+1}. It is assumed that p

satisfies the conditions for the mean value theorem for definite integrals, and since a point must exist somewhere in Ω_i with pressure equal to P_i^{n+1}, then any hypocentre inside this cell can have this pressure.

Accelerated updates are the main advantage of avoiding a linear interpolation for each seed. A linear interpolation, although simple for structured cells, is much less straightforward when the effect of fractures and wells and of their orientations needs to be considered. When the errors from the suggested approach need to be diminished, then employing a finer mesh with smaller $|\Omega_i|$ sizes can be sufficient.

The set of seeds, for which the failure criterion (12) is satisfied given $\mathbf{P}^{n+1}$ is collected and the synthetic catalogue of the DFHM simulation is updated with their hypocentres and their moment magnitudes. Their source time is the simulation moment to which the $(n+1)$-th time step corresponds. Here, seeds must not be triggered twice, nor are their properties affected by previously triggered seeds; however, these criteria could easily be changed.

For the sake of simplicity, gravitational effects are neglected, and the sampled properties of the seeds stay the same throughout a DFHM simulation. The b-value of the Gutenberg-Richter distribution is assumed constant and not dependent on stress, in contrast to what is proposed in Goertz-Allmann and Wiemer (2013). Stress changes due to earthquake-earthquake interaction (i.e. static Coulomb stress changes) are neglected, nor do we consider poro-elastic effects, although again both effects could be readily added to the framework.

3.2.3 Updating the deterministic flow model

We assume disc-shaped ruptures Ω_s that are centred around each sampled $\bar{\mathbf{x}}_s$, and the corresponding $\bar{\mathbf{n}}$ is normal to them. A constant stress drop $\Delta\tau$ is considered for all events. In this case, Eshelby (1957) has shown that the radius of these discs can be expressed as

$$\bar{R}_s = \sqrt[3]{\frac{7 \cdot \bar{M}_0}{16 \cdot \Delta\tau}}, \tag{25}$$

where $\bar{M}_0$ is derived from the right-hand side of eq. (11). Also, the same post-rupture mechanical aperture $\bar{b}^f = b^f$ and permeability $\bar{k}^f = k^f$ are considered for all events.

Only triggered seeds with $\bar{R}_s > R_{min}$ are explicitly treated by HFR-Sim as a discrete fracture, where R_{min} is a user-defined value. A disc-shaped fracture is meshed around $\bar{\mathbf{x}}_s$, and hydraulic properties b^f and k^f are assigned to it. It is important to ensure that R_{min} is large enough to ensure that fractures penetrate more than one damaged matrix, otherwise ill-posed systems of equations are possible.

For the rest of the triggered seeds with $\bar{R}_s \leq R_{min}$, a homogenisation is performed, and the

permeability of damaged cells increases as the number of triggered hypocentres inside them increases. The permeability of the damaged cells increases in a stepwise manner according to its density $\rho_3^{'}$. Initially, the hypocentres inside each grid are divided into the maximum possible number of subsets. Each subset must have $\rho_3^{'} > \rho_c^{'}$, where $\rho_c^{'}$ is a user-defined value. Once exceeded, an interconnected network of discs inside the cell is more likely than an unconnected one. Permeability equal to k^f is considered for all such interconnected subsets and a homogenisation approach similar to that suggested by Oda (1985) is employed, where each subset increases k^d by a portion of k^f equal to the portion of the void volume V^i that corresponds to the subset. For the sake of simplicity, the percolation criterion is $\rho_c^{'} = 3.6$ for cells that are not penetrated by a discrete fracture and $\rho_c^{'} = 1.8$ otherwise. The former value is close to the converged solution for a scenario where discs can have any orientation, their sizes follow a power law and the diameters of the discs can be up to the grid-block size (Mourzenko et al. (2005)).

Finally, HFR-Sim updates all transmissibilities C_{ij} in eq. (17) and the next timestep of the DFHM can be simulated.

4 EXEMPLARY DETERMINISTIC DFHM SIMULATIONS

We now use our hybrid EGS reservoir simulator DFHM described in sections 2 and 3 for single-scenario (one forward run) calculations, to highlight potentials and limitations of the model, but also to gain insights into the EGS reservoir creation process and its relationship to induced seismicity. In section 5, we will then consider probabilistic calculations that use numerous Monte Carlo realisations to capture uncertainties.

Two different EGS scenarios are considered and simulated with DFHM. In subsection 4.1, the results from simulating both the creation and the production phase of an EGS doublet are presented. In subsection 4.2, induced seismicity is modelled for a stimulated but abandoned well that stays shut for several years after its stimulation, inspired by the situation of the Basel EGS project, where seismicity restarted some years after shut-in of the well in 2011.

All properties of the initial geological model considered both here and in the next section are summarised in Tables A1-A3. This initial geological model is in agreement with many of the initial properties of a real stimulated EGS reservoir, the abandoned EGS reservoir BS1 in Basel (Häring et al., 2008). However, note that we are here not aiming for an optimised fit to the Basel observations, but use Basel as a known starting point for simulations of realistic systems. In this and the next section, all shown pressures are over-pressures; i.e. the pressure change compared to the initial pressure of the formation $p(t \leq 0)$.

4.1 DFHM simulation for the creation and the production phase of an EGS doublet

The scenario of a doublet is considered, where the casing shoes of the two parallel wells are 250m apart from each other and are aligned to the direction of maximum horizontal stress. Each well is stimulated with a strategy similar to the stimulation strategy of BS1, but somewhat idealised by smoothing the observations. The total volume of injected water is the same as for the stimulation of BS1, that is approximately 12,000 m2. Initially, one well is stimulated, then this well stays shut for a period of few days, and then the stimulation of the second well begins. Seismicity from both well stimulations is modelled for a period of 40 days. The DFHM simulation of the creation phase returns the simulated pressure logs for the casing shoe (CSH), a simulated seismicity, and a discrete fracture network (DFN). Then, the DFHM is employed for simulating the production phase for the resulting DFN and for a fixed pressure difference of 20 MPa between the two stimulated wells.

In Fig. 2, the selected injection strategy in litres per second is plotted in the top row (2A), while the results from the DFHM model are plotted below it both for the creation and the production phase.

The simulated CSH pressure (2B) is unrealistically high during the first day of each stimulation and it exceeds 500 MPa, but it quickly reduces to more realistic values as the number of seismic events increases. Such unrealistically high pressures are due to the rather coarse mesh around the well source, due to the misrepresentation of the geological model close to the well, and due to the fact that a stimulation strategy in the end is going to be the one that the reservoir allows.

Seismicity does not occur immediately with the injection onset, but the first induced events occur after a few hours (2 B and C). The rate of seismicity is the highest during injection; however, earthquakes also continue in the days after shut-in, decaying gradually as also observed in natural systems. Note that the second stimulation produced only about 70 percent of the number of events simulated in the first one. However, it also produced the largest event simulated, a magnitude Mw = 3.2, by chance the same magnitude as observed in Basel in 2006. The injectivity index of the wells, the ratio of injected water per unit of overpressure, drops with seismicity and with each new injection step.

In Fig. 3, snapshots of the simulated hypocentres in map view and cross-sectional view, as well as the overpressure distribution and the traces of the sheared fractures are plotted for 6 times. These times correspond to the 6 vertical dashed grey lines in the well logs shown in Fig. 2. As expected, seismicity initially occurs only close to the well and in locations where a significant increase of overpressure occurred. Note that the shape of the events cloud is

somewhat complex and ragged, and it would look quite different for different realisations of stochastic seed sets. This is an expected and desired consequence of the randomly drawn seeds and their ability to channel overpressure, as already explained in Figure 1. The resulting distribution of overpressure is even less homogeneous, since it depends both on the sheared DFN and on the duration of diffusion inside a large fracture. The fronts of overpressure and of hypocentres do not travel with the same speed. By the end of the first stimulation ($t = T_2$), overpressures are simulated for distances up to 2 times further than the furthest hypocentre. For the shut-in period from T_2 until T_3, the Kaiser effect is reproduced, i.e. the rate of seismicity close to the second well is significantly reduced.

By the end of the 40-day period, both seismicity clouds have merged into one cloud, seismicity is modelled both away and in between the wells, and the overpressure front is smoother as pressure diffuses outwards.

The final enhanced DFN created by the stimulation and its enhanced hydraulic properties can now be employed for simulating the production phase for different flow rates between the wells. The impedance between the two wells is estimated at 2.75 $l/(sMPa)$ and the temperature of the injected water is set to 60^oC. The production rate that maximises E_e over a period of 40 years is found at 19.5 l/s, following a line optimisation with a Brent algorithm where the pressure between the two casing wells cannot exceed $\Delta P_{max} = 20\ MPa$.

At the bottom frames of Fig.2, the temperatures of the fluid produced for F_{max} and for the optimum flow rate are plotted, as well as the breakthrough curve of the optimum rate of E_e. In the latter plot, the rate of E_e is plotted for three different conversion efficiencies

$$\eta \approx \begin{cases} 1. - (T_c + 273.)/(T_h + 273) \\ 0.00052 \cdot T_h + 0.032 \\ 0.078795 \log\left(4183 \cdot (273. + T_h)4183\right) - 1.00081 \end{cases} \tag{26}$$

where T_c and T_h are the temperature of the injected and of the produced water, respectively. Also plotted is the Carnot's theoretical maximum η, and two are empirical fits for η (Jefferson W. Tester Brian J. Anderson & Jr., 2006; Zarrouk & Moon, 2014). All optimisations are performed for the logarithmic fit of η Zarrouk & Moon (2014) and power generation is not allowed for produced temperatures below 100°C. The latter restriction is not only realistic but also necessary given that η exceeds the Carnot's maximum for low T_h.

Also, the time evolution of the temperature of the produced water is simulated with HFR-Sim for this scenario. Snapshots of the evolution of temperature are shown in Fig. (4) for the surface that connects the two wells. In these snapshots, the rapid decline of the produced T_h is explained; although the realised set of discrete fractures creates an interconnected network

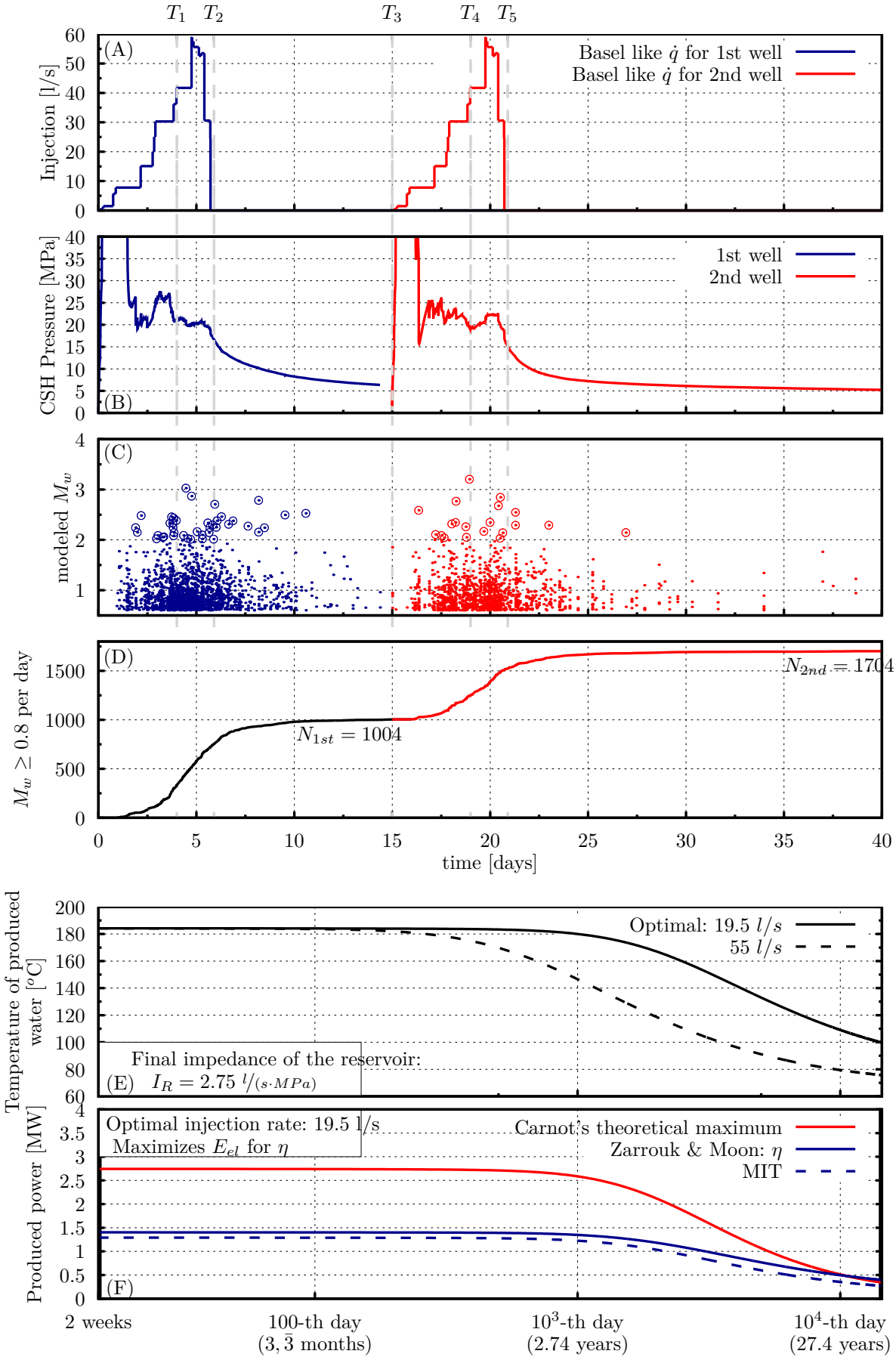

Figure 2. Well logs, synthetic catalogue and evolution of power generation from the demonstrative simulation of an EGS doublet.

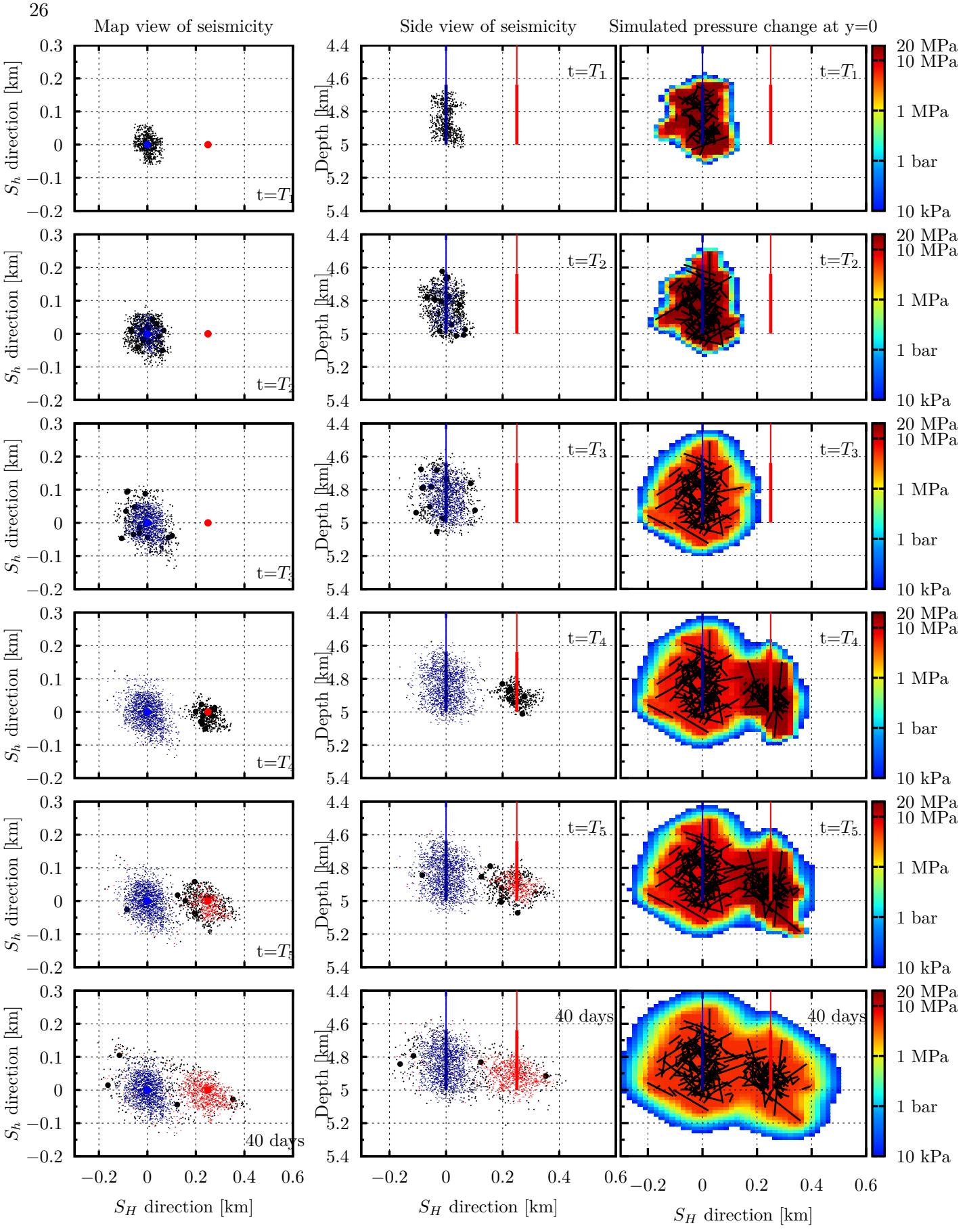

Figure 3. Snapshots of hypocentres and of pore-pressure evolution from the demonstrative simulation of an EGS doublet. Hypocentres that happened during the corresponding time segment are coloured as black dots and are bigger for felt events ($M_w \geq 2$). The cloud of past seismicity is coloured blue for the first well and red for the second.

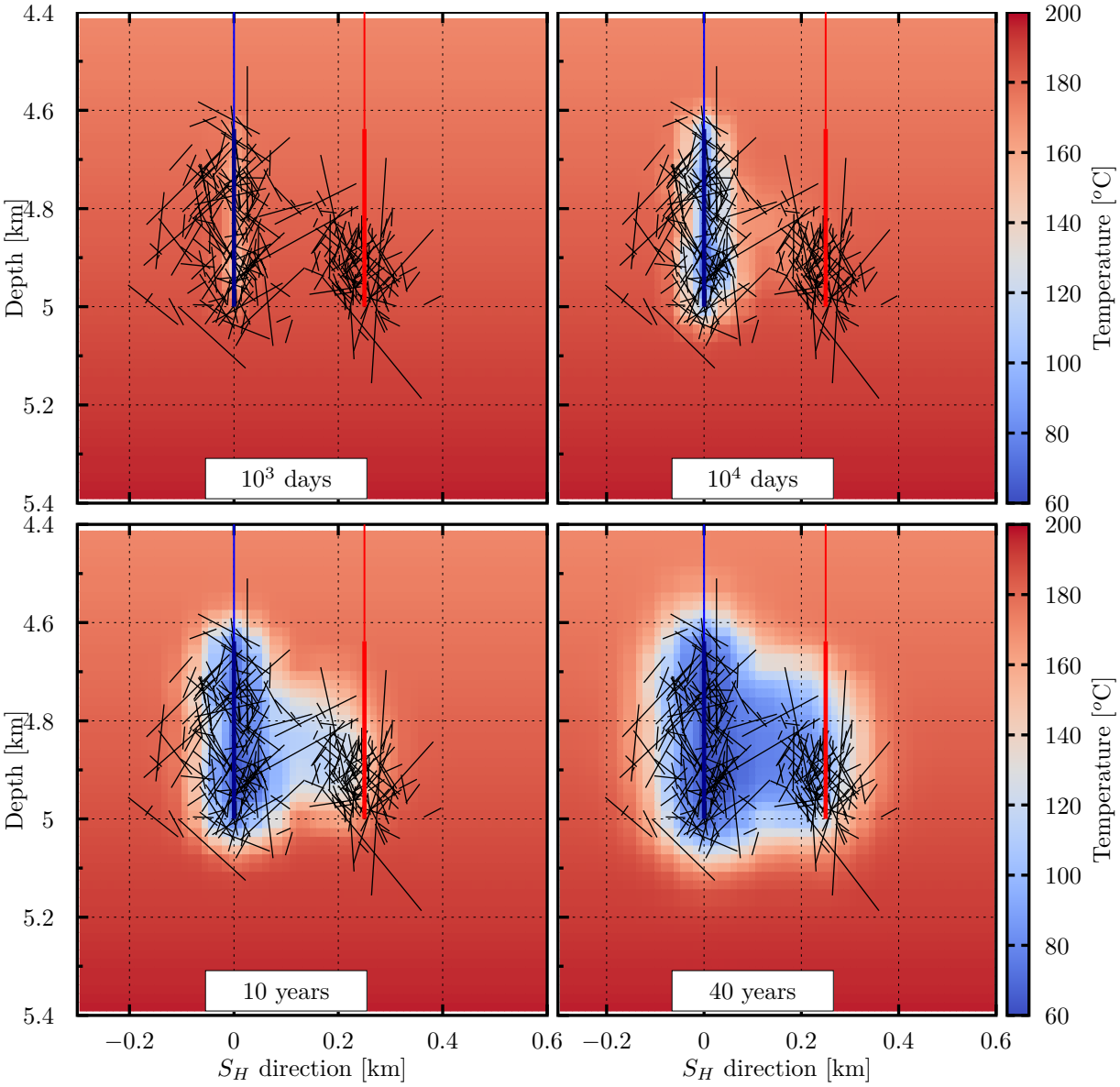

Figure 4. Cross-sectional view of the reservoir (at the surface $y = 0$), colour-coded are 4 snapshots of the temperature distribution. Black lines indicate the projected traces of the discrete fractures that ruptured during reservoir creation.

of fractures that penetrates both wells, overall the flow is not dispersed at the whole reservoir and a short channel, or shortcut, is created instead. The hot rock around this path cools down more rapidly due to the large flow rates that it circulates and it accelerates the decline of T_h. Note that the flow rate of 55 l/s is for ΔP_{max} and is the value at which the Brent algorithm initialises.

4.2 Long-term seismicity evolution

We now evaluate the long-term behaviour of seismicity after short-term, high-pressure injections into crystalline basement rocks. There is limited empirical data, because few high-pressure injections in basement rock exist in the first place, good and long-term monitoring is rare and in some cases the wells then entered the operational phase. Observations from Cooper Basin (Baisch et al., 2006) and Basel (Bachmann et al., 2011; Herrmann et al., 2019) suggest, however, that seismicity may continue for many years, a consequence of continued pressure diffusion and a result of the fact that many faults have been brought close to failure by the injection. Bachmann et al. (2011) estimated that in Basel, seismicity is decaying exponentially, indistinguishable from the almost universally observed Omori-type decays following tectonic mainshock (Ogata, 1999). This decay was estimated in 2011 by Bachmann et al. (2011) to last about 15 years, an observation confirmed by the seismicity still ongoing in 2018 (Herrmann et al., 2019), So far, however, to our knowledge, the long-term decay of seismicity following fluid injection has not been modelled. Here, the DFHM is employed for testing the effect of diffusion on the long decay of induced seismicity.

We consider the 2006 injection in Basel, now assuming that only one well is stimulated for 6 days, kept shut for 6 hours and ultimately opened indefinitely. The parameters for the stochastic model are provided in Tables A2 and A3. If we use the the same frictional parameter $\delta\mu$ considered in subsection 4.1, seismicity decays away quite rapidly. To make the model reproduce a decay lasting years, we consider a smaller friction parameter $\delta\mu$, 50 times less than the one considered in subsection 4.1. This represents in essence a more "critically stressed" scenario.

The resulting simulated long-term decay of seismicity is plotted in Fig. 5 in a log-log plot of number of events as a function of time. The observed seismicity from Basel (Kraft & Deichmann, 2014) is also plotted. Although a proper calibration of DFHM's parameters was not performed, the DFHM still returns a long-term decay of seismicity that resembles the Omori-like decay going on for years, as observed in Basel. After the 3rd day following the shut-in and re-opening, the seismicity of the DFHM decays with a decline rate close to -1.3, which is close to the decay exponent rate reported for Basel (Bachmann et al., 2011). Therefore, our model is inherently able to reproduce the long-term behaviour of seismicity, suggesting that the observed long-term seismicity is caused by continued migration of the overpressure cause by the injection.

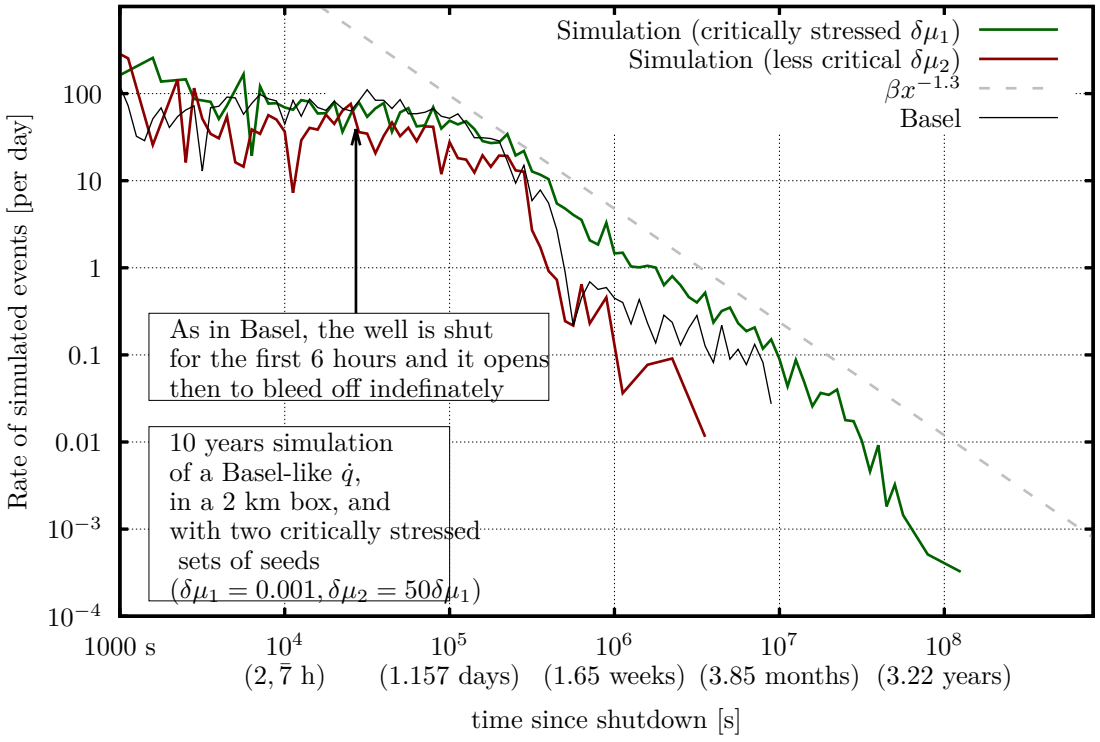

Figure 5. Long-term decay of seismicity simulated with the hybrid model and for well operations similar to Basel. The green and red lines show two models with different assumed criticality of faults. For comparison purposes, the seismicity from Basel is at the same plot (black line).

5 EXEMPLARY PROBABILISTIC DFHM SIMULATIONS

The DFHM model is now employed for Monte Carlo (MC) simulations to assess the efficiency of three different stimulation strategies, as well as to characterise the variability expected in seismicity and reservoir productiveness. MC simulations allow us to study numerous realisations of a system, and alternative strategies, even if we have only one realisation in nature. Therefore, they allow us to not only characterise the mean behaviour of a system, but also its variance around the mean as well as the sensitivity to input parameters.

The considered initial geological model and the numerical parameters are again as described in Tables A1-A3. We set up the model such that it considers several of the observations collected before stimulating the Basel-1 well. First of all, the well's orientation is close to the true trajectory. Secondly, the fracture Ω_1^f represents the ruptured surface of the M_w 1.4 event, a known event recorded by the Swiss Seismological Service in 2006 and during the cementing of BS1. This event was found very close to both the casing shoe and to an important fracture through which a significant portion of injected water entered the reservoir. Initial hydraulic

parameters for the damaged matrix and Ω_1^f belong to the family of solutions for which HFR-Sim reproduces the reservoir's behaviour before the stimulation (Ortiz R. et al., 2011). The density of fractures $\dot{\rho}_f$, the stress orientation and the orientation of the ruptured planes take into account the reported geophysical logging from the Basel-1 well (Valley & Evans, 2009; Ziegler et al., 2015). The measured vertical, maximum and horizontal stresses at the bottom of the well are considered to be the mean three principal stresses everywhere in Ω (Häring et al., 2008). The critical stresses for seed faults are limited to $\bar{p}_f \leq 30\ MPa$, considering this as the maximum overpressure that the pumps used in Basel could deliver.

Each simulation uses the identical modelling parameters but is based on a newly generated set of random seed fractures. While the overall density of faults is kept constant, the location, orientation, size and stress state of all seed faults are randomly assigned in each simulation run, representing the natural variability in these largely unknown parameters during stimulation. In addition, MC simulations make it possible to not only determine the optimal distance and strategy for stimulating the two wells of an EGS doublet, but also to assess the trade off between seismic safety and electricity or heat generation. It would be possible to extend MC simulations to also consider the uncertainty in each model parameter, a step needed for a full uncertainty quantification in a probabilistic hazard study. Here, however, we want to focus on the effect of the DFN.

In section 5.1, the injection strategy employed for the stimulation of Basel-1 is considered and compared with the results of two alternative stimulation strategies, often referred to by the community as 'soft stimulation' strategies (Meier et al. (2015); EU project DESTRESS, 2016-2020). Statistical analysis of the three MC simulations makes it possible to compare these strategies with regard to the induced seismicity they create on average, and to assess whether the differences observed are statistically significant. Next, we evaluate the average effectiveness of different risk mitigation (or intervention) strategies for quickly mitigating risk in simulations (section 5.2). Finally, the underling processes related to one of the soft-stimulation strategies is verified in section 5.3.

Note that the aim here is not to describe the current status of the reservoir in Basel or to reach conclusions about its future. Only the orientation of Ω_1^f, the density of seeds $\dot{\rho}_s$, and the b-value of seismicity are based on observations collected during the stimulation ($2nd$ day of stimulation). The rest of the input parameters were processed from data collected before the stimulation itself and almost no rigorous effort for inverting the parameters has been performed. In a way, results shown here for the stimulation strategy of Basel-1 are nothing more than a very late forecast of induced seismicity in Basel-1.

5.1 Seismicity expected from Basel-1 and soft stimulation strategies

Here, three different injection strategies are considered, and induced seismicity is forecasted for each of them. The first stimulation strategy q_1 is the one from the Basel-1 well, which is also considered in section 4.1 and where injection happens always throughout the single, 400-m long open segment of the well. The 'soft' q_2 and 'softer' q_3 injection strategies consider a multi-stage injection with four stages. In this case, the four quartiles of the well are each stimulated separately, with a one-day delay before stimulating the next segment, and with the same injection profile for each segment. More precisely, the profile of the injection at each quartile of the soft scenario is equal to one quarter of the profile q_1 and hence $q_2 \approx (q_1/4)$. The profile of the injection of the softer scenario considers an eighth of q_1, but it lasts twice as long as q_1, and therefore $q_3 \approx (q_2(t/2)/2)$. Eventually, the same cumulative volume of almost $12,000$ tons of water is injected in all three scenarios; the injection strategies are plotted in the top row of Fig. 6.

Induced seismicity due to each stimulation strategy is forecasted for $M = 250$ different sets of random seeds' parameters. However, the same set of randomly drawn seeds is employed here for each of the strategies. This enables one-by-one comparison of scenarios. As an example, the simulated well logs and synthetic catalogues are plotted in Fig. 6 for three DFHM simulations. The simulated pressure, the shape of the seismic cloud and the sequence of induced seismicity are quite different, even though the same set of seed faults is considered in all three scenarios.

To allow for a more quantitative analysis, we now simulate the first 90 days for each strategy and repeat the calculation for 250 sets of seeds. The normalised density distribution of simulated events as a function of distance and time is plotted in Fig. 7 for all three stimulation strategies. The density plots confirm the general patterns already visible in the individual simulations shown in Fig. 6 with four peaks of seismicity visible for the multi-stage stimulations. For all three stimulation strategies, seismicity is concentrated within 200 m of the well but can occur as far out as 450 m, and the softer q_3 stimulation appears to be limited to 400 m, but this difference is based on very few events and may not be statistically significant.

During the injection, the seismicity overall and the densest seismicity (in orange and red) migrate outwards, and a Kaiser effect is visible once the injection stops. The first decile of seismicity (area in orange) continues dispersing outwards when injection stops, but only for a few days. After that, seismicity is more likely at intermediate distances than in the furthest or nearest stimulated regions.

It is noteworthy that in the multi-stage simulations q_2 and q_3, the shape of the density plots changes with every new segment, illustrating that they are affected by the previous

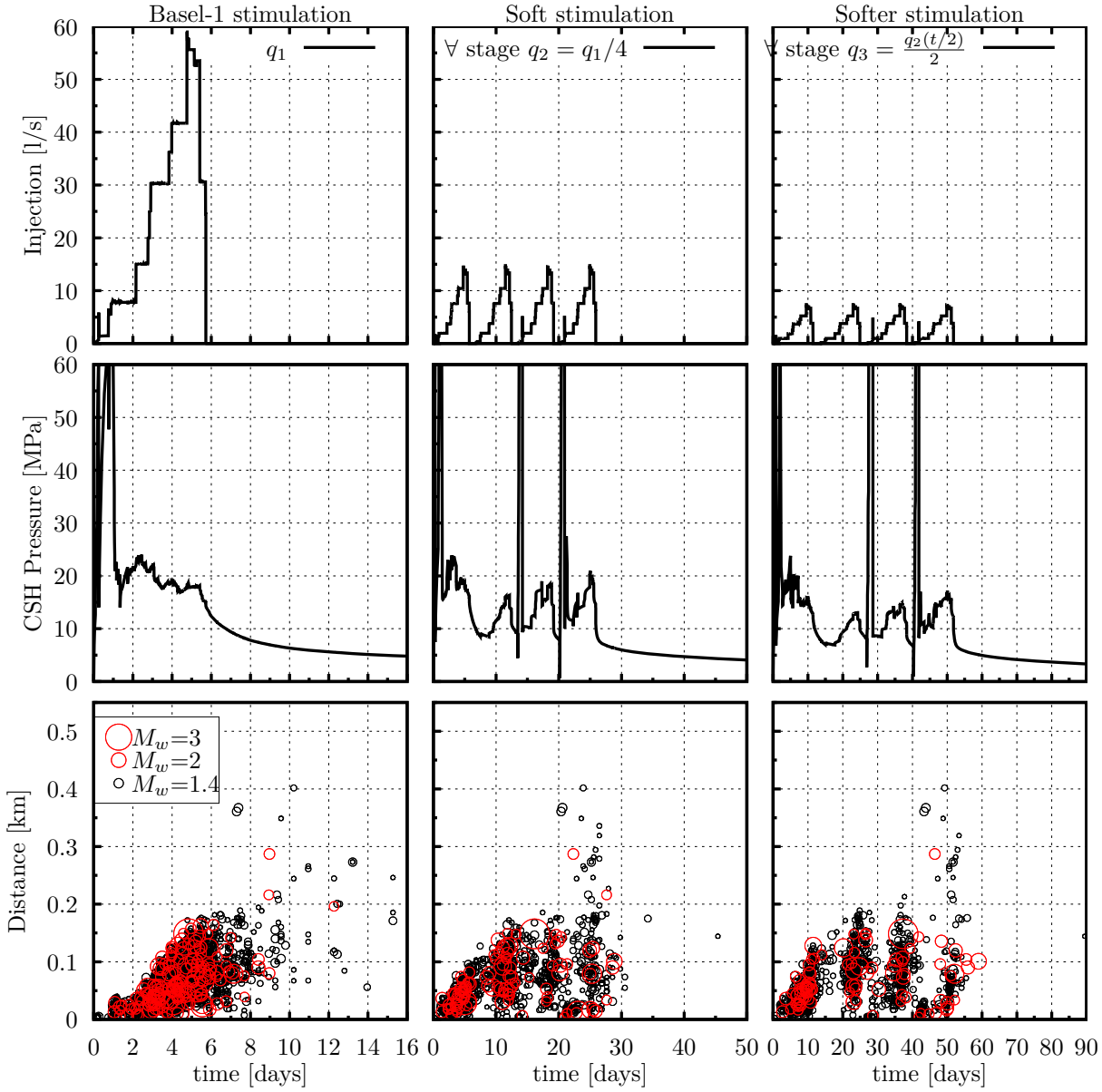

Figure 6. Simulated well logs in terms of pressure (top row), CSH Pressure (middle row) and time-distance migration of simulated seismicity (bottom row) for the same set of seeds and for three different stimulation strategies (three columns). Note that the time axis is scaled with the duration of the stimulation in each column.

segment. Specifically, seismicity in stages 2-4 does not always begin near the well but can also resume at some distance, while each stage reaches out to even further distances. For example in q_3, seismicity on the 17th day is more likely to resume where the previous stage ended than near the well, while on the 29th day, seismicity is equally likely close to and away from the well but not in between. Ruptured surfaces that penetrate the next stages can explain

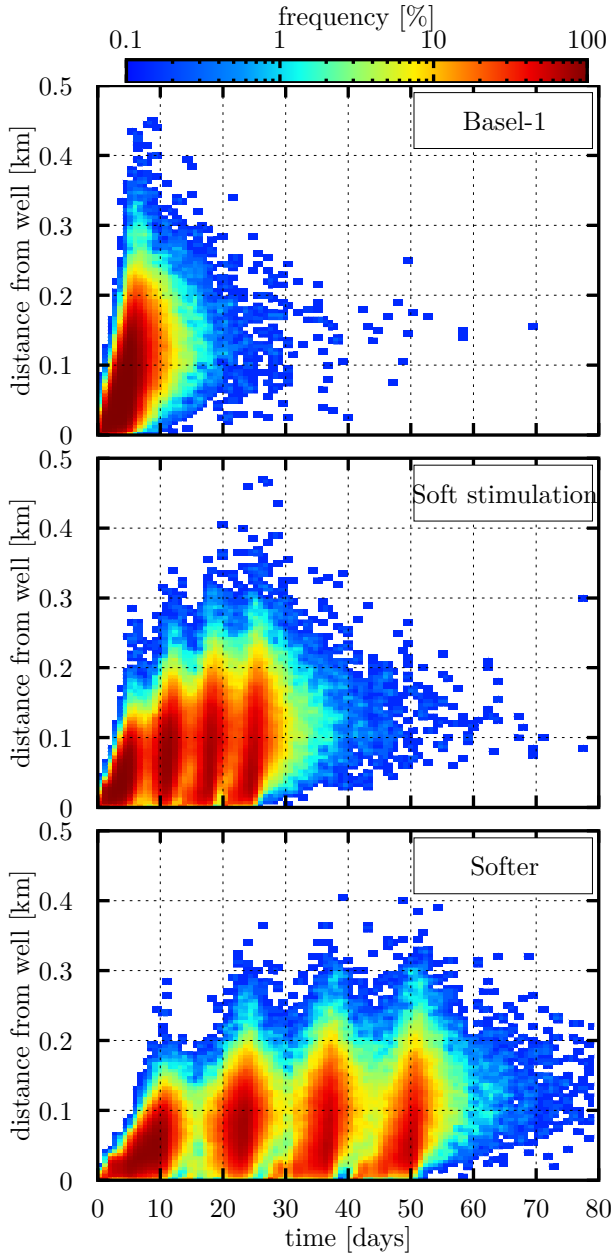

Figure 7. Distribution of the frequency with which seismicity is modelled at a certain distance from the injection well and at a certain moment given the considered stimulation.

situations where seismicity seems to resume from where the previous stage ended. Repeated events are not considered and a seed can fail maximum once.

Interestingly, the outward migration of the quantiles is closer to linear than to square-root dispersion. The square-root migration is expected from normal diffusion where a single diffusivity exists (e.g. Shapiro & Dinske (2009)) and linear migration when seismicity disperses with a constant speed. Such steady, linear migrations are not unexpected in geothermal reservoirs and have been attributed to several mechanisms such as elastic stress transfer, slow

and aseismic slip, fracture creation, thermal effects and changes in the permeability structure (Goebel & Brodsky, 2018). Here, changes in the permeability structure and pore-pressure diffusion are sufficient mechanisms for linear migration.

We now analyse the result with respect to its implications for the maximum expected earthquake and the number of events above a given magnitude threshold. Following the suggestion by Gischig & Wiemer (2013), we differentiate between the maximum possible event (the true $Mmax$ used typically in PSHA studies), the maximum observed in a given stimulation and the maximum expected, defined as the mean of the maximum observed in multiple simulations. The maximum possible earthquake in our simulation is set to the tectonically possible maximum at magnitude 6.5; however, randomly drawing such a result is extreme unlikely. Gischig & Wiemer (2013) and also van der Elst et al. (2016) have shown that hybrid models will reproduce the observation by McGarr (1976) that the maximum observed magnitude scales linearly with the logarithm of the total injected volume. Our DFHM results likewise result in this scaling relationship, as in Fig. 8a. The median and the range of the maximum expected magnitude as a function of the cumulative injected volume for the Basel-1 stimulation shows a linear increase with volume during the injection, reaching a mean expected magnitude of about 3.31. However, with 5 percent probability also a magnitude of 3.7 is possible. Thus, the observed maximum of Mw=3.2 is well within the simulated range. Once the injection stops, the maximum expected increases by about 0.1 to 0.2 magnitudes (Fig. 8) due to the continued and exponentially decaying seismicity. Note that we do not assume a stress-dependent b-value, which would increase the chance of large events after shut in (Goertz-Allmann & Wiemer, 2013). We also do not directly model earthquake-earthquake interactions, which have been shown by Catalli et al. (2016); Rinaldi & Nespoli (2017) to contribute a substantial fraction of additional events, nor we consider repeating events and overlapping ruptured surfaces.

Comparisons of the same quantiles from the two softer stimulations showed little deviation from the Basel-1 case, and hence these stimulations are not plotted. Stimulations deviate more clearly in the post-injection, where a significant increase of M_w^{max} is less likely when stimulating in segments than in the Basel-1 scenario. This increase of M_w^{max} due to post-injection seismicity in the Basel-1 scenario is captured in Fig 8a, where the vertical step change at the end of each quantile is for the M_w^{max} at the end of the 90th simulated day.

A clear differentiation of the strategies is observed both for the mean number of simulated events and for the dispersion of seismicity, as can be seen in Fig. 8b, where again each discontinuous vertical jump quantifies the increase during stages and at the end of the

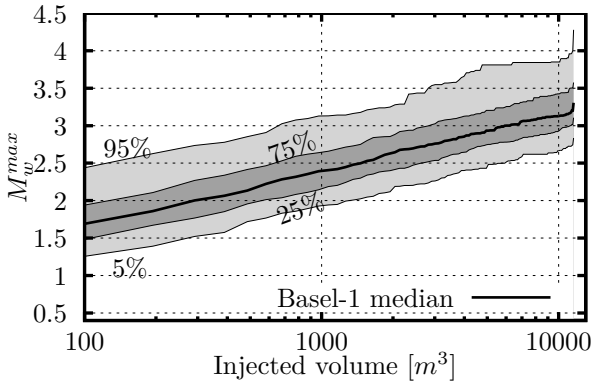

(a) McGaar-like plot for the Basel-1 like simulations

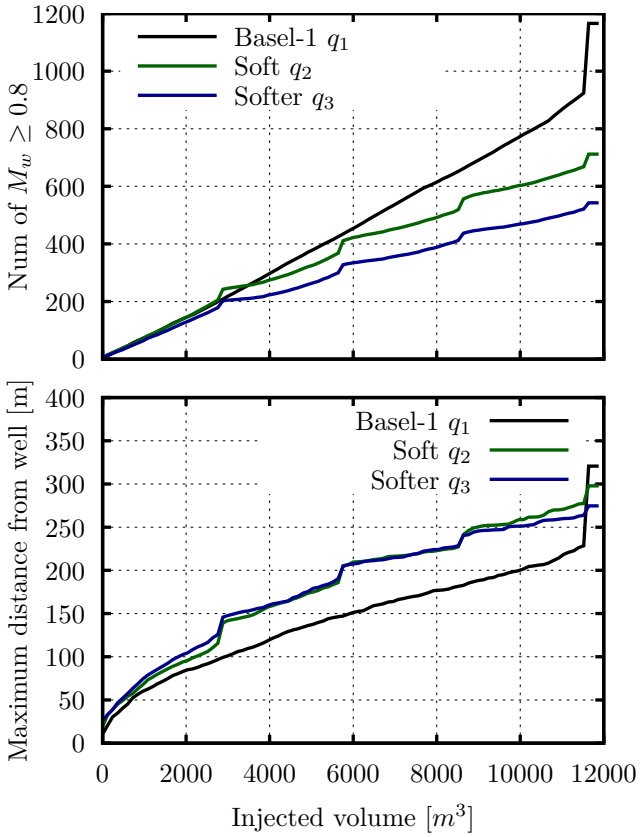

(b)

Figure 8. In (a), the probable M_w^{max} at each moment of the DFHM simulations is plotted as a function of the logarithm of the total injected volume and for the Basel-1 stimulation. In (b), the mean number of seismic events with $M_w \geq 0.8$ and the mean migration of seismicity away from the well are plotted for the total injected volume. The discontinuous increase at the end is due to the induced seismicity after the injection and while the well is shut.

90th simulated day. For each first segment, the expected number of events increases linearly with the injected volume and with similar rates. With each new segment, however, this rate decreases and hence the expected seismicity depends both on the injected total volume and on how it is injected. Overall, both soft stimulations generate in our simulation fewer seismic events both during and after injection, with the softer stimulation demonstrating the lowest total rate of seismicity of water volume, about 550 events, so only half of the one for the massive, single-stage injection. Note that after shut in, the softer stimulations have only a fraction of the seismicity of the full Basel-1 stimulation.

Also in Fig. 8b, the mean dispersion of seismicity is plotted with the total injected volume. On average, seismicity for the same injected volume migrates the slowest with Basel-1. However, migration in post-injection overcompensates this so that the Basel-1 stimulation reaches out the furthest.

The correlation between the stimulation strategy and some of the characteristics of seismicity is analysed further in Fig. 9. All 3×250 simulated scenarios are represented by a dot in the space of M_w^{max}, number of events N_{eq}, and furthest migration for the seismicity. All stimulation strategies can create large events, and clearly visible is that the q_1 strategy produces substantially more events, However, the most interesting feature of Fig. 9 is the at first counter-intuitive observation that for each of the strategies, the number of stimulated events is inversely correlated with the maximum magnitude. We interpret this observation such that if larger events with magnitudes of 3.5 occur during the stimulation, they will dominate the fracture network, pressure distribution and flow. Pressure will be distributed over a larger region but at lower overpressures, creating fewer events. The newly created fault will itself increase void volume and reduce pressure, leading to few events. However, these findings remain somewhat speculative, because ruptures of a magnitude of 3.5 or larger can exceed the computational domain and hence their effects may be incorrectly represented here. Such boundary issues explain the bifurcation of M_w^{max} with distance; in other words, the model returns a positive correlation between them when boundary effects due to large M_w^{max} are absent. Interestingly though, the considered injection does not affect the relationship between these two properties and it depends mainly on the seeds sampled with $\mathfrak{f}_{\bar{\mathbf{\Theta}}}$.

We now establish whether the difference in the total number of observed events is statistically significant. We plot the returned kernel density of N_{eq}, M_w^{max}, and the distance for the three injection strategies in Fig. 9. Considering that both the b-value and the cumulative injected volume is the same for all scenarios, a seismogenic index model (Shapiro et al., 2010) would predict similar mean numbers and variations. However, we observe that stimulations

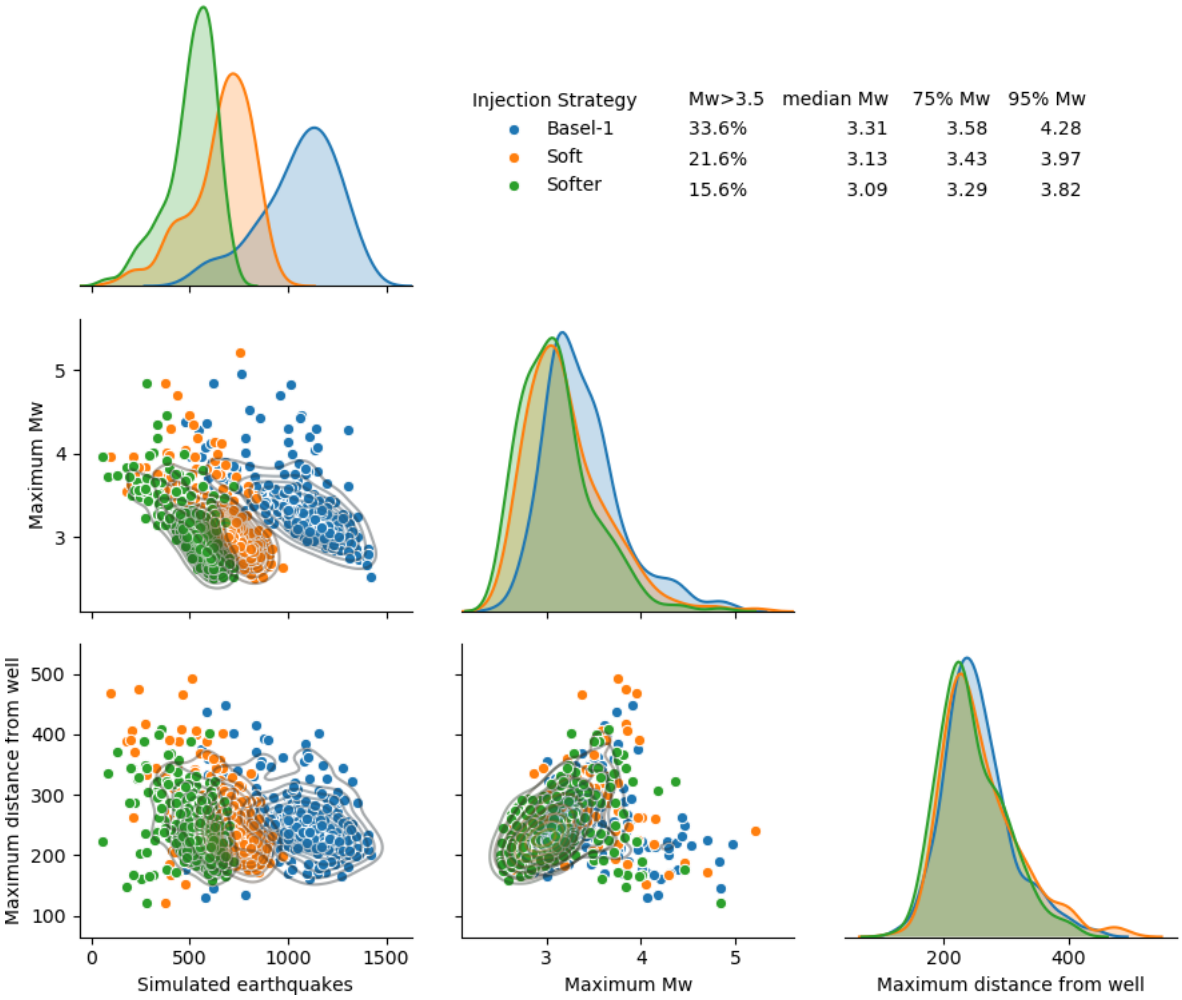

Figure 9. The pairwise relationship for the simulated number of events N_{eq}, the maximum simulated event M_w^{max} and the furthest hypocentre are plotted for all scenarios and all injection strategies in the lower diagonal, while the kernel-density estimate of each parameter by using Gaussian kernels is plotted in the upper diagonal. Percentiles of M_w^{max} and the probability of $M_w^{max} > 3.5$ are provided for each strategy.

q_2 and q_3 are substantially lower in their total number of events than q_1 and the distributions significantly different with >99.9 percent confidence. All three densities have a negative skewness which decreases as the stimulation becomes softer. On the other hand, the skewness is positive both for M_w^{max} and the furthest hypocentre, but injection strongly affects only the former. In summary, according to our DFHM simulation, the least hazard should be expected from softer multi-stage simulations as defined in q_3 and the most seismic hazard results from Basel-1-like stimulations. Later it will be shown that multi-stage stimulations can generate more electricity than Basel-1 too.

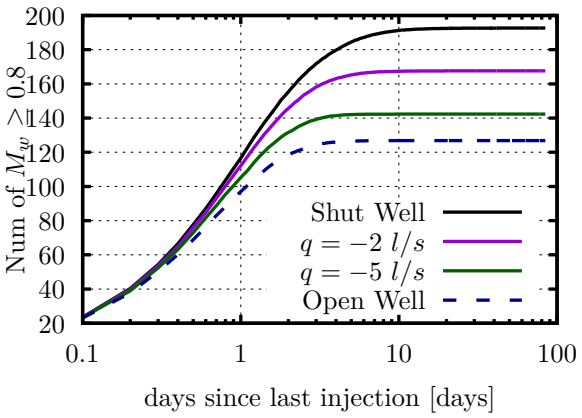

Figure 10. Expected seismicity following a Basel-1 like stimulation, when four different risk mitigation strategies are considered.

5.2 Strategies for rapid mitigation of risk after a Basel-1-like stimulation

Risk mitigation measures applied in near real time are an important part of Health and Safety assessment and of reducing the overall risk of any EGS project. Past EGS projects have relied on a traffic-light system that will reduce or terminate injections once a certain magnitude or vibration threshold is reached (e.g., Baisch et al. (2019); Häring et al. (2008)). As seismicity will not stop immediately after stopping the injection (e.g. Fig. 5), action must be taken early enough to avoid the predefined acceptance threshold potentially being exceeded. The more conservative a traffic-light system is set up, the safer the operation will be; however, it will also have a reduced chance of being commercially viable. A key parameter in setting up traffic lights is the effectiveness of mitigation action, and so far there have been few studies addressing these questions based on reservoir simulations. Opening the well immediately after the injection is considered to be an efficient way of reducing induced seismicity at that time (Baisch et al., 2006; McClure & Horne, 2011); however, it has been argued after the Basel project, for example, that immediate shut in is not a good strategy, since sudden stress changes can trigger larger events.

We perform MC simulations for four distinct choices for mitigating risk. The considered risk mitigation scenarios are: one scenario where the well is kept shut indefinitely ($q = 0\ l/s$), two scenarios where fluids are produced at rates $q = -2\ l/s$ and $q = -5\ l/s$ for a period of 10 days before shutting the well indefinitely, and a scenario where the well is left open to bleed off. In the last mitigation scenario, q is a function of the overpressure at the casing shoe and of the atmospheric conditions at the surface. Here, a linear relationship is assumed for modelling bleed-off conditions, where q is proportional to the overpressure at the casing shoe

and changes with rate $I = -0.8\ l/s$ per MPa of overpressure. In this way, the casing shoe relaxes towards hydrostatic pressure.

The number of simulated events after the injection of 12,000 m^3 of water and for all considered scenarios for mitigating risk are plotted in Fig. 10.

Out of the four risk mitigation strategies, namely keeping the well shut in, is found to be the least efficient with the largest number of post-injection events modelled with it. Opening the well is found to be the most efficient with approximately 35% less post-injection seismicity than keeping the well shut. Neither of the two strategies with steady production achieves such a reduction, although the cumulative water volume extracted is larger than when the well is opened. We interpret this result such that the high water production immediately after opening the well, when the seismicity rate is highest, is the key to reducing seismicity rates quickly. We suspect that production with 10 l/s or more would be as efficient or even more so than the open-well strategy, but it may not be operationally easy to achieve. This result also highlights the need for rapidly implementing risk mitigation strategies.

Finally, an MC simulation is performed with the DFHM for the scenario, where injection continued as originally planned. In this scenario, 90 l/s is injected for another 6 days. This is the maximum rate that the pumps in Basel could inject in that time. All 250 simulated scenarios returned $M_w^{max} \gg 3.5$. This finding confirms the findings of the SERIANEX Risk Study (Baisch, S., Carbon, D., Dannwolf, U., Delacou, B., Devaux, M., Dunand, F., Jung, R., Koller, M., Martin, C., Sartori, 2009) and subsequent analysis (Gischig & Wiemer, 2013) reporting that establishing an EGS given the selected injection strategy and the seismic response to injections was and is not feasible.

5.3 Optimal strategy for stimulating EGS doublets successfully

Finally, we evaluate the maximum electricity that can be safely extracted for each of the stimulation strategies presented in subsection 5.1, as well as the necessary seismicity for achieving certain energy production targets. We perform MC simulations considering EGS doublets where the two wells of each doublet reach the same depth, have the same orientation and are always stimulated with the same strategy.

For the first well, we use the same MC simulations presented earlier in Fig. 6. This setup is appropriate because it shows many common desired features, i.e. long dispersion of seismicity, $M_w^{max} < 3.5$, and many common large fractures in their sheared DFN. The final pressure solution, the sheared DFN and the resulting hydraulic properties from each sample and each injection strategy are the initial conditions for the respective MC simulations afterwards.

Six discrete locations for the second well are now considered, and $M = 30$ different sets of seeds are initialised and comparisons between different inter-well distances and stimulation strategies are almost always possible, although larger errors around the mean are expected with such low M. DFHM simulations and optimisations are performed for each set of seeds, for each stimulation strategy and for each discrete location of the second well. Out of these $M \times 3 \times 6 = 540$ DFHM simulations, an equal number of random DFNs are employed and out of them an equal number of optimal evolutions of produced temperature is obtained by finding with a Brent algorithm the maximum electricity, as in section 4.1. Therefore, the expected electricity from each stimulation is the maximum value out of all these optimal values.

The results of these 18 MC simulations and optimisations are shown in Fig. 11, where electrical power is always averaged over a period of 25 years, and with the conversion efficiency η suggested by Zarrouk & Moon (2014) and in eq. (26).

Expected seismicity (Fig. 11a) increases with the distance between the two wells, up to the point where the two stimulations are independent of each other and a similar mean seismicity is expected from each. Increasing the distance between wells from 250 to 700 m will increase the seismicity by 50-100 percent, depending on the choice of the stimulation strategy. The Basel-1-like stimulation strategy q_1 is, as expected, again the most seismically active, while the least seismicity is expected from the softer stimulation q_3, reduced by about half compared with q_1.

Contrary to seismicity, which never decreases with increasing distance, the expected impedance of the reservoir shown in Fig. 11b involves a local minimum around 350 m to 445 m. The impedance seems to depend less on injection strategy, especially when there is a larger well spacing. Note that the forecasted impedance is estimated only from the sheared DFN and for the resulting permeability. Frequently, a target impedance of 0.1 $MPa/(l/s)$ is considered for EGS (Rybach, 2010). This impedance is not achieved by any of the DFHM simulations and for the properties of Table A3. Reaching this target impedance would likely require pre-existing highly permeable structures within the reservoir, which is a piece of information that if it had been known in 2006 could have been included by considering these structures in the initial fracture model on top of which the fractures from the seeds are superimposed.

The distances returning the largest produced electricity in MW (11c) coincide broadly with the distances for lowest impedance. Optimal distances are within the range [280 m, 440 m] for stimulations with q_2 and q_3, and [360 m, 520 m,] for q_1. Neglecting seismic hazard as a limiting factor, either of q_1 and q_2 can be the stimulation with maximum expected power.

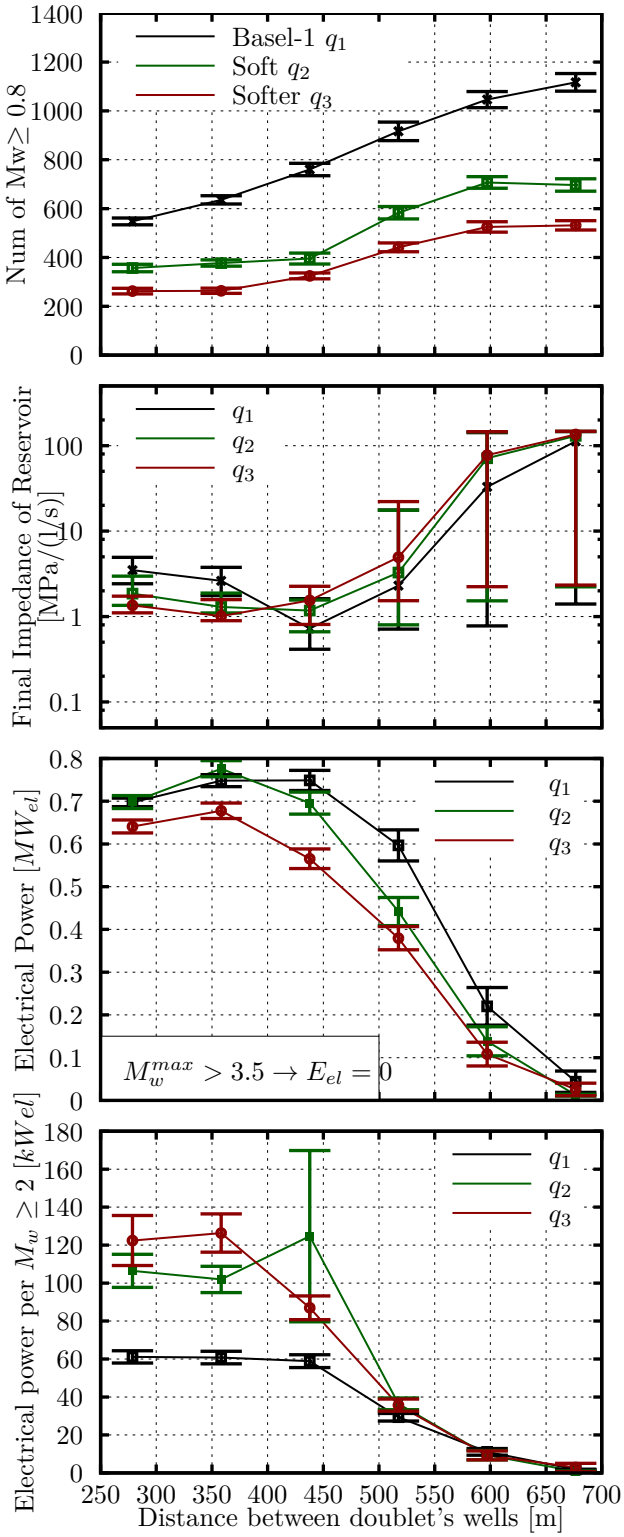

Figure 11. From top to bottom, the expected number of events, the expected impedance between the wells of the doublet, the expected electrical power over a period of 25 years, and finally the expected number of $M_w \geq 2$ events per generated electrical power unit are plotted for each setting. Contrary to the rest of the figures where the bars show the error, bars around the mean impedance show the sample size.

Stimulation strategies q_1 and q_2 are always more productive when compared with q_3. Note that systems with well distances of more than about 500 m are rapidly producing very little electricity energy, because of the high impedance of the reservoir and resulting energy needs for pumping. Also noteworthy is the fact that at 0.8 MW the overall maximum energy output of this systems under ideal conditions remains well below the targets for the Basel EGS (3 MW electric). This target was very unlikely to be reached with $11,000\ m^3$, unless a large and highly permeable structure happened to pre-exist between the wells, a scenario not considered here in the initial reservoir model.

In a final normalisation effort shown in Fig. 11d now adds the seismicity aspect to the optimisation. We ask the question how to generate the maximum electrical power with the minimum number of felt or potentially damaging earthquakes. Therefore, we normalise the power output by the number of magnitude M>= 2.0 events needed on average to stimulate the reservoir. Using this metric, soft stimulation strategies q_2 and q_3 are about twice as effective when compared with q_1, and distances $< 400\ m$ are preferable.

6 DISCUSSION AND CONCLUSIONS

6.1 Uniqueness of DFHM

The ability to reliably forecast the seismicity and transmissivity generated when injecting fluids under high pressure into granitic underground is critical for the successful deployment of EGS technology (Hirschberg et al., 2015). Prominent and costly failed projects over the past 15 years (Giardini, 2009; Lee et al., 2019) and also the current lack of upcoming EGS projects illustrate the fact that currently, forecasting tools are unable to achieve this goal.

The 3D DFHM model and reservoir simulator introduced in the previous sections represents in our judgement a novel and highly advanced coupled reservoir simulator approach. Its uniqueness lies in a combination of features targeted to enhance its usefulness for a wide range of applications, and builds on these enhancements:

(i) DFHM implements a hybrid approach that balances accurate representation of first-order physical processes (such as fractures and diffusion) with stochastic elements that make computations feasible but most of all allow us to represent the inherent uncertainties in our knowledge of in-situ fault locations, orientation, sizes and stress/strength conditions. Similarly to other hybrid models (Goertz-Allmann & Wiemer, 2013; Gischig & Wiemer, 2013; Karvounis et al., 2014; Rinaldi et al., 2015; Jin & Zoback, 2017; Langenbruch et al., 2018), DFHM considers seismicity as a Markovian process with a transition probability, the PDF of

which is $f_{\bar{\Theta}}$, which encapsulates all of the uncertainty and is conditioned on pore-pressure distribution. Contrary to other hybrid models, DFHM simulates pore-pressure distribution with an EGS simulator that can consider individual fractures and fracture networks of almost any geometrical complexity and returns accurate solutions of the pore-pressure diffusion problem. This ability allows for a much more realistic (in terms of geology and physics) representation of relevant processes in EGS reservoirs.

(ii) DFHM can be used deterministically (e.g. Figs 3 and 4) be calibrated to a set of observations for an understand of the process, or to explore scenarios; however, it can also be used probabilistically by deploying Monte Carlo simulations spanning a wide range of uncertainties (e.g. Figs 7 and 8). The ability to represent uncertainties is critically needed not only as the input for probabilistic seismic hazard assessment when low-probability but high-consequence events dominate the risk profile (Mignan et al., 2015; Broccardo et al., 2020; Bommer et al., 2015) but also for meaningful sensitivity studies and for the difficult decision-making process when there are uncertainties in near real time. Monte Carlo simulation allows us for example to judge whether observed differences between injection strategies (Fig. 8), for example, are statistically significant.

(iii) DFHM is able to also provide solutions for temperature (Fig. 4) and heat revenues (Fig. 11), using the same fracture network, thus making it possible to address directly and consistently the challenging problem of balancing energy output and seismic safety.

(iv) The DFHM code is computationally optimised such that it can run and scale on high-performance computers, thereby making it possible to address major problems of substantial temporal and spatial complexity rapidly. Speed is a critical parameter if real-time applications as part of data-driven adaptive traffic light systems (Király-Proag et al., 2018; Grigoli et al., 2017) are tackled. Real-time risk assessment is indeed a critical community need (e.g. Lee et al. (2019), because the a priori uncertainties before stimulation are very considerable (Broccardo et al., 2020) and can only be reduced substantially once data from the actual stimulation become available (Broccardo et al., 2017; Mignan et al., 2017). The code can also be extended to include additional physical interaction mechanisms such as poro-elasticity or Coulomb stress interactions. Note that while we have focused here on processes related to EGS, the overall DFHM approach can be applied or extended to other GeoEnergy applications.

The combination of these features sets DFHM apart as a sophisticated and holistic reservoir simulator that allows users to address a wide range of problems related to EGS systems and beyond. In this publication we have illustrated its capabilities, as well as some of the limitations, which are discussed in more detail below. Overall, we feel that DFHM advances

the state of the art in modelling coupled reservoir processes substantially, opening up new capabilities for scenario modelling, process understanding, probabilistic analysis and real-time decision support. The DFHM simulator is available under a GNU GPL V3 licence from the authors. Obviously, the DFHM model also has numerous limitations, which we discuss in the final section of this paper.

6.2 Implications of DFHM numerical experiments: multi-stage, soft stimulations and mitigation strategies

In this study we performed a number of numerical experiments with DFHM, not only to demonstrate its usefulness and limitations but also to address important and unresolved questions related to the creation and operation of EGS reservoirs. A first important result of our analysis is the fact that, based on our DFHM modelling, multi-stage stimulations ('soft stimulations') are more efficient in creating an EGS reservoir even if they inject the same total fluid volume. Multi-stage stimulations have been proposed as a more efficient and more controlled way to stimulate a reservoir (McClure & Horne, 2014; Meier et al., 2015), and our study is the first to our knowledge that provides a quantification of this effect. Our simulations show that multi-stage stimulation will create only about half of the seismicity (Figs 8b and 9) and offer lower reservoir impedance (Fig. 11b) and therefore can produce more electricity and heat for a given acceptable seismic risk. This finding is quite different from the forecast made by existing statistical or hybrid reservoir models that assume the seismicity in essence to be a site-specific constant (e.g. a 'seismogenic index' (Mignan et al., 2017; Shapiro et al., 2010)). In our simulation, Basel-like 'massive' stimulations that do not target individual well segments are up to 2 times more likely to exceed $M_w^{max} > 3.5$ than multi-stage stimulations, where a constant b-value is assumed. In other words, Basel-like stimulations are only half as likely to lead to a successful project that will maintain public acceptance and would allow a return on investment. The optimal distances for the multi-stage injections are found to be $\approx 360\ m$ (Fig. 11); there is only a small and statistically insignificant advantage of 'softer' (i.e. injection q_3) stimulations that will inject with lower flow rates and pressures over a longer time (Fig. 11). Note that we did not consider the Coulomb stress or poro-elasticity-based interaction of stages due to creep or opening of cracks. Adding these mechanisms, as suggested in the limitation sections, would be an important future enhancement to our modelling capability.

An additional benefit of multi-stage stimulation can be seen from Figure 8, namely that the seismicity occurring after the stimulation is over is significantly less and also the continued spatial growth of the reservoir is less than for a single stage. For massive injections q_1, about

20% of seismicity occurs after the termination of the injection, while for strategies q_2 and (especially) q_3, this fraction is less then 2%. The continued migration of the fluid overpressure and seismicity likewise is substantially less (Figure 8b). Together, these factors result in the desired feature of a higher degree of 'controllability' of a stimulation, because once mitigation actions are taken, the reaction of the system is more immediate. We also speculate (but have not yet tested this hypothesis) that the surprisingly (i.e. decade-) long 'aftershock' sequence seen in Basel observations and in our models (Figure 5) would be substantially shorter (i.e. a more rapid decay parameter) for multi-stage, softer stimulations. The physical reason for all these differences is connected to the lower overpressure needed in multi-stage and softer stimulations (Figure 7): it takes a long time before rock volumes under high levels of overpressure in tightly packed basement rocks return to background levels of pressure through pressure diffusion.

With respect to the best mitigation strategies when seismicity exceeds threshold levels, our simulations show that the strategy of opening the well immediately after the injection leads to the most rapid reduction in the induced seismicity rate (Fig. 10). Our modelling thus supports the decision in 2006 to open the BS1 well in Basel. Pumping out from the well can be effective too if pumping rates are high enough, and it can be beneficial in the long run when natural bleed off is lower. Besides, we demonstrate that pore-pressure diffusion is a sufficient mechanism for explaining decade-long sequences of induced seismicity as observed in Basel (Fig. 5).

In summary, our results suggest that future EGS systems should focus on multi-stage stimulations and consider lower-pressure, but longer-lasting injections. Our simulations are limited to only four adjacent segments; however, we also show that the expected electricity revenue given that the reservoir impedance is quite limited, at about 0.7 MW (Figure 11). More stages, using for example horizontal or inclined well set-ups, should offer additional benefits with respect to limiting seismic hazard, increased controllability while also making it possible to scale up to commercially more interesting systems capable of generating 3-5 MW of electrical energy. Ideally, multi-stage stimulations would also be able to identify and avoid unsuitable fractures, fractures that would result in above-average seismicity or in thermal shortcuts.

6.3 Implications of DFHM numerical experiments: Understanding of the process

Our simulations show that in realistic fracture networks such as the one modelled in Figs 6-7, seismicity during the injection migrates in a steady linear way outwards from the injec-

tion point. Our modelling results can be explained by pore-pressure diffusion combined with permeability enhancement in a 3D fractured medium. Normal diffusion in a single diffusivity medium would result in square-root migration outwards, and has been proposed as a relevant mechanism (e.g. Shapiro & Dinske (2009)). Our modelling results are more in line with (Goebel & Brodsky, 2018), who observed linear migration in a number of injection cases, including Basel, but did not pinpoint a single mechanism, and hypocentre accuracy is a limiting factor in observational studies. Our results confirm numerically that anomalous 3D diffusion, which consists of several convoluted small 2D linear diffusion processes, can explain such deviations from the square-root migration and we speculate that this may be common or even the dominating mechanism in reservoirs. Finer DFHM simulations with a larger sample of seeds would be needed to reach conclusions regarding the expected rule for migration and its variance.

Especially for Basel-style massive stimulation, three approximately linear trends are qualitatively observed. The first one is the increase of the distance with the highest likelihood to be stimulated as the injection duration increases with time (Fig. 7). The other two are the increase of the expected number of events N_{eq} with the injected volume and the increase of the median for M_w^{max}.

In our modelling, not all combinations of N_{eq}, M_w^{max} are equally expected. As a matter of fact, a negative correlation is observed because when a large M_w^{max} is simulated, then a lesser number of triggered events is simulated afterwards (Fig. 9). This correlation cannot be explained by methods like the Extreme Value Theory (van der Elst et al., 2016) or the seismogenic index (Shapiro et al., 2010) that consider N_{eq} as a variable independent of earlier M_w^{max}.

Our modelling results also confirm the assessment of the SERIANEX Risk Study (Baisch, S., Carbon, D., Dannwolf, U., Delacou, B., Devaux, M., Dunand, F., Jung, R., Koller, M., Martin, C., Sartori, 2009) that the prematurely ended stimulation in Basel in 2006 was insufficient to create a commercially viable reservoir. If the same injection was to be repeated for the second well BS-2, then the resulting EGS could at best reach half the target impedance and half of the target generation of electrical energy.

The linear relationship between N_{eq} and the injected volume, scaled by a site-specific constant (e.g. a seimogenic index), is a common assumption in many first-order methods for predicting induced seismicity rates (Shapiro et al., 2010; Mignan et al., 2017). This simple model is surprisingly very much in line with observations (Király-Proag et al., 2016, 2018; Mignan et al., 2017). However, our DFHM simulation shown in Figures 7-11 allow for a more

differentiated analysis. A linear relationship between seismicity and fluid volume injected exists only for the Basel-1 massive stimulation scenario (Fig. 8b), and is very much in line with the data. In this case, the seismicity response to a cubic metre of injected water is represented effectively by a constant. However, when modelling multi-stage injections, this linear response breaks down (Figure 8b) and fewer events than expected occur in later stages. We speculate that in multi-stage injections, interactions with already stimulated areas could decrease the seismicity rate. The injection rates and stimulation strategy influence the number of events, but seem to have little influence on the stimulated volume.

We observed a wide variation of possible N_{eq} in different Monte Carlo runs (Figure 9b), namely variations by about a factor of two. This variability is a consequence of the fact that even with identical fault density and stressing condition, small differences in fault orientation and connectivity can make a substantial difference to the pressure distribution (Figure 1). This suggests that a seismogenic index must also vary quite substantially even when injection is happening into near identical reservoirs.

6.4 Forecasting long-term EGS operations, potentials and limitations

Stakeholders prioritise differently the challenges related to induced seismicity since they seek reliable decisions for many different operations. For instance, regulators and the public may mainly be interested in forecasting the M_w^{max} and N_{eq}, while for insurance industries the primary focus may be on convincingly classifying a damaging M_w^{max} as induced or triggered, and for EGS investors it will be on the levelised cost of electricity expected (Mignan et al., 2019). Issues arise when the meta-models applied by different stakeholders are too loosely correlated, making their combination less likely to be true. Holistic approaches like the DFHM return strongly correlated multi-objective forecasts since a common hidden mechanism is considered.

As is the case with all models and meta-models, they return useful forecasts only after inverting the model's parameters and tuning its hyper-parameters. The tuning of the hyper-parameters could be done by finding from their space the values that minimise a cost function like the mean squared error of the forecast (also known as a 'Brier score') or by maximising the conditional probability

$$\mathbb{P}\left(\mathbf{f}|U,\mathcal{S}_{:t}\right) = \frac{\mathbb{P}(\mathbf{f}|\mathcal{S}_{:t}) \cdot \mathbb{P}(U|\mathbf{f},\mathcal{S}_{:t})}{\mathbb{P}(U|\mathcal{S}_{:t})}, \tag{27}$$

for the cases where the utility forecast U is realised due to $\mathbf{f}$, $\mathbb{P}(\mathbf{f}|\mathcal{S}_{:t})$ is the marginal distribution of the transition between states, $\mathbb{P}(U|\mathbf{f},\mathcal{S}_{:t})$ the likelihood-base rate of how well

the forecasts' hyper-parameters discriminate between different outcomes and different past situations, and $\mathbb{P}(U|\mathcal{S}_{:t})$ a marginal distribution that indicates how well the tuned forecast distinguishes between different situations. As in Murphy & Winkler (1987), the forecast is considered calibrated when the expected utility that depends on the marginal distribution of final states $\mathbb{P}(\mathbf{f})$ equals U.

Here, examples of parameters are the properties of the fluid, of the solid materials, of the well and of the reservoir. Many of these can be assessed through traditional techniques of reservoir engineering (e.g. an initial model) or their range of probable values is small and is characterised by low entropy even when they are stochastic (e.g. the post-shearing aperture of a fracture b^f). There are also parameters like the b-value that have irreducible uncertainty and can be assessed by their maximum likelihood or through a Bayesian approach (Broccardo et al., 2017). Examples of hyper-parameters of the DFHM are the parameters controlling the shape of the transitional PDF $\mathfrak{f}_{\bar{\boldsymbol{\Theta}}}$ such as the distribution of fracture points $\mathbf{x}_s$, as well as the cohesion and the friction considered. Last but not least, the number of degrees of freedom and boundary conditions at the model's boundaries can also be treated as hyper-parameters, since this is a forecasting problem and not an inversion problem where accurately reproducing past observations is important. Especially when real-time forecasts are sought, the increase in the maximum forecasting likelihood may not justify the computational load required by handling a more complex model and reaching the same state of forecasting ability $\mathbb{P}\left(\mathbf{f}|U,\mathcal{S}_{:t}\right)$.

Single-phase flow is a significant limitation of the current model. Although multi-phase flow can be accurately modelled with embedded DFMs (Hajibeygi et al., 2011; Ţene et al., 2017), here such an extension would be associated with a significant increase in the model's parameters since the saturation of each phase would need to be inverted and calibrated for all degrees of freedom. In the simulations presented here, these starting conditions were never really an issue since an intact reservoir was considered with hydrostatic conditions, and the principle of superposition could be employed for the single-phase pore pressure.

Discretisation issues arise both because of the well model, which is inappropriate for tiny time steps when diffusivity is very low compared with the grid size, and because of the homogenisation of small induced seismicity events. Employing coarse models of DFHM for inverting the observed wellhead pressure is not advised. Also, forecasts with coarse DFHM are expected to be loosely correlated when the same problem is simulated with a fine model. Especially because of the well model, coarse models would initialise their branching process differently.

Mechanical modelling has not been employed anywhere in DFHM. Given that pore-

pressure diffusion is the main mechanism for induced seismicity in EGS, other mechanisms have not been considered. Neither induced seismicity due to stress transfer nor induced seismicity due to thermal contraction have been considered, although these two mechanisms are also important in EGS stimulations. Without loss of generality, these mechanisms could be introduced into future versions, either with a dynamically changing transitional PDF or with deterministic modelling of the elastic effects (Deb & Jenny, 2017a,c), where the latter makes it possible to consider ruptures with overlapping surfaces. This would require a better characterisation of fractures and more complex shapes both for the seeds and for the initial fracture network, since fractures are found in nature in many shapes (Peacock et al., 2016).

Finally, the presented DFHM cannot provide answers to important seismological questions such as what the maximum possible M_w is in a reservoir and whether an event is triggered or induced. The answers in both of these cases need to be assumed by the transitional PDF. Here, a common Guttenberg-Richter law was considered for triggered and induced events.

ACKNOWLEDGMENTS

The work presented here was developed for the purposes of the Advanced Traffic Light System RT-RAMSIS devised by the Swiss Seismological Service in ETH Zurich and by Geo-Energie Suisse AG. Funding for the development was provided by the Swiss Federal Office of Energy and by the Swiss Innovation Agency, for the projects GeoSim and RAMSIS-RT, respectively. We also wish to thank Dr. Peter Meier, Dr. Andres Alcolea Rodriguez, Dr. Nicholas Deichmann, Dr. Toni Kraft, Dr. Antonio Pio Rinaldi, Dr. Andreas Fink, Dr. Marco Favino, and Luca Scarabello for all our constructive discussions with thems.

References

AbuAisha, M., Loret, B., & Eaton, D., 2016. Enhanced Geothermal Systems (EGS): Hydraulic fracturing in a thermo-poroelastic framework, Journal of Petroleum Science and Engineering, 146, 1179–1191.

Atkinson, G. M. & Eaton, D. W., 2020. Developments in understanding seismicity triggered by hydraulic fracturing, Nature Reviews Earth & Environment, 1(May).

Bachmann, C. E., Wiemer, S., Woessner, J., & Hainzl, S., 2011. Statistical analysis of the induced Basel 2006 earthquake sequence: introducing a probability-based monitoring approach for Enhanced Geothermal Systems, Geophysical Journal International, 186(2), 793–807.

Baisch, S., Weidler, R., Voros, R., & Jung, R., 2006. A Conceptual Model for Post-Injection Seismicity at Soultz-souz-Forets, GRC Transactions, 30, 601–605.

Baisch, S., Vörös, R., Rothert, E., Stang, H., Jung, R., & Schellschmidt, R., 2010. A numerical model for fluid injection induced seismicity at Soultz-sous-Forêts, International Journal of Rock Mechanics and Mining Sciences, 47(3), 405–413.

Baisch, S., Koch, C., & Muntendam-Bos, A., 2019. Traffic Light Systems: To What Extent Can Induced Seismicity Be Controlled?, Seismological Research Letters, 90(3), 1145–1154.

Baisch, S., Carbon, D., Dannwolf, U., Delacou, B., Devaux, M., Dunand, F., Jung, R., Koller, M., Martin, C., Sartori, M., 2009. Deep Heat Mining Basel: Seismic Risk Analysis, SERIANEX Group., Tech. rep., SERIANEX Group. Departement für Wirtschaft, Soziales und Umwelt des Kantons Basel-Stadt, Basel.

Berre, I., Doster, F., & Keilegavlen, E., 2019. Flow in Fractured Porous Media: A Review of Conceptual Models and Discretization Approaches, Transport in Porous Media, 130(1), 215–236.

Berre, I., Boon, W. M., Flemisch, B., Fumagalli, A., Gläser, D., Keilegavlen, E., Scotti, A., Stefansson, I., Tatomir, A., Brenner, K., Burbulla, S., Devloo, P., Duran, O., Favino, M., Hennicker, J., Lee, I. H., Lipnikov, K., Masson, R., Mosthaf, K., Nestola, M. G. C., Ni, C. F., Nikitin, K., Schädle, P., Svyatskiy, D., Yanbarisov, R., & Zulian, P., 2021. Verification benchmarks for single-phase flow in three-dimensional fractured porous media, Advances in Water Resources, 147(September 2020).

Blessent, D., Therrien, R., & Gable, C. W., 2011. Large-scale numerical simulation of groundwater flow and solute transport in discretely-fractured crystalline bedrock, Advances in Water Resources, 34(12), 1539–1552.

Bommer, J. J., Crowley, H., & Pinho, R., 2015. A risk-mitigation approach to the management of induced seismicity, Journal of Seismology, 19(2), 623–646.

Bour, O., 2002. A statistical scaling model for fracture network geometry, with validation on a multiscale mapping of a joint network (Hornelen Basin, Norway), Journal of Geophysical Research, 107(B6), 2113.

Box, G. E. P. & Muller, M. E., 1958. A Note on the Generation of Random Normal Deviates, The Annals of Mathematical Statistics, 29(2), 610–611.

Broccardo, M., Mignan, A., Wiemer, S., Stojadinovic, B., & Giardini, D., 2017. Hierarchical Bayesian Modeling of Fluid-Induced Seismicity, Geophysical Research Letters, 44(22), 11,357–11,367.

Broccardo, M., Mignan, A., Grigoli, F., Karvounis, D., Rinaldi, A. P., Danciu, L., Hof-

mann, H., Milkereit, C., Dahm, T., Zimmermann, G., Hjörleifsdóttir, V., & Wiemer, S., 2020. Induced seismicity risk analysis of the hydraulic stimulation of a geothermal well on Geldinganes, Iceland, Natural Hazards and Earth System Sciences, 20(6), 1573–1593.

Bruel, D., 2007. Using the migration of the induced seismicity as a constraint for fractured Hot Dry Rock reservoir modelling, International Journal of Rock Mechanics and Mining Sciences, 44(8), 1106–1117.

Candela, T., Wassing, B., ter Heege, J., & Buijze, L., 2018. How earthquakes are induced, Science, 360(6389), 598–600.

Catalli, F., Rinaldi, A. P., Gischig, V., Nespoli, M., & Wiemer, S., 2016. The importance of earthquake interactions for injection-induced seismicity: Retrospective modeling of the Basel Enhanced Geothermal System, Geophysical Research Letters, 43(10), 4992–4999.

Deb, R. & Jenny, P., 2017a. Finite volume-based modeling of flow-induced shear failure along fracture manifolds, International Journal for Numerical and Analytical Methods in Geomechanics, 41(18), 1922–1942.

Deb, R. & Jenny, P., 2017b. Modeling of shear failure in fractured reservoirs with a porous matrix, Computational Geosciences, 21(5-6), 1119–1134.

Deb, R. & Jenny, P., 2017c. Finite volume-based modeling of flow-induced shear failure along fracture manifolds, International Journal for Numerical and Analytical Methods in Geomechanics, 41(18), 1922–1942.

Egya, D. O., Geiger, S., Corbett, P. W. M., March, R., Bisdom, K., Bertotti, G., & Bezerra, F. H., 2019. Analysing the limitations of the dual-porosity response during well tests in naturally fractured reservoirs, Petroleum Geoscience, 25(1), 30–49.

Ellsworth, W. L., 2013. Injection-induced earthquakes., Science (New York, N.Y.), 341(6142), 1225942.

Eshelby, J. D., 1957. The Determination of the Elastic Field of an Ellipsoidal Inclusion, and Related Problems.

Evans, K. F., Moriya, H., Niitsuma, H., Jones, R. H., Phillips, W. S., Genter, A., Sausse, J., Jung, R., & Baria, R., 2004. Microseismicity and permeability enhancement of hydrogeologic structures during massive fluid injections into granite at 3 km depth at the Soultz HDR site, Geophysical Journal International, 160(1), 389–412.

Farkas, M. P., Hofmann, H., Zimmermann, G., Zang, A., Bethmann, F., Meier, P., Cottrell, M., & Josephson, N., 2021. Hydromechanical analysis of the second hydraulic stimulation in well PX-1 at the Pohang fractured geothermal reservoir, South Korea, Geothermics, 89.

Gaucher, E., Schoenball, M., Heidbach, O., Zang, A., Fokker, P. A., van Wees, J.-D., & Kohl,

T., 2015. Induced seismicity in geothermal reservoirs: A review of forecasting approaches, Renewable and Sustainable Energy Reviews, 52, 1473–1490.

Giardini, D., 2009. Geothermal quake risks must be faced., Nature, 462(7275), 848–9.

Gischig, V., Wiemer, S., & Alcolea, A., 2014. Balancing reservoir creation and seismic hazard in enhanced geothermal systems, Geophysical Journal International, 198(3), 1585–1598.

Gischig, V. S. & Wiemer, S., 2013. A stochastic model for induced seismicity based on non-linear pressure diffusion and irreversible permeability enhancement, Geophysical Journal International, 194(2), 1229–1249.

Gneiting, T., Balabdaoui, F., & Raftery, A. E., 2007. Probabilistic forecasts, calibration and sharpness, Journal of the Royal Statistical Society. Series B: Statistical Methodology, 69(2), 243–268.

Goebel, T. H. W. & Brodsky, E. E., 2018. The spatial footprint of injection wells in a global compilation of induced earthquake sequences, Science, 361(6405), 899–904.

Goertz-Allmann, B. P. & Wiemer, S., 2013. Geomechanical modeling of induced seismicity source parameters and implications for seismic hazard assessment, GEOPHYSICS, 78(1), KS25–KS39.

Gough, B., 2009. GNU Scientific Library Reference Manual - Third Edition, Network Theory Ltd., 3rd edn.

Grigoli, F., Cesca, S., Priolo, E., Rinaldi, A. P., Clinton, J. F., Stabile, T. A., Dost, B., Fernandez, M. G., Wiemer, S., & Dahm, T., 2017. Current challenges in monitoring, discrimination, and management of induced seismicity related to underground industrial activities: A European perspective, Reviews of Geophysics, 55(2), 310–340.

Grigoli, F., Cesca, S., Rinaldi, A. P., Manconi, A., López-Comino, J. A., Clinton, J. F., Westaway, R., Cauzzi, C., Dahm, T., & Wiemer, S., 2018. The November 2017 M w 5.5 Pohang earthquake: A possible case of induced seismicity in South Korea, Science, 360(6392), 1003–1006.

Gutenberg, B. & Richter, C. F., 2010. Magnitude and energy of earthquakes, Annali di Geofisica, 53(1), 7–12.

Hainzl, S. & Ogata, Y., 2005. Detecting fluid signals in seismicity data through statistical earthquake modeling, Journal of Geophysical Research: Solid Earth, 110(5), 1–10.

Hajibeygi, H., Karvounis, D., & Jenny, P., 2011. A hierarchical fracture model for the iterative multiscale finite volume method, Journal of Computational Physics, 230(24), 8729–8743.

Häring, M. O., Schanz, U., Ladner, F., & Dyer, B. C., 2008. Characterisation of the Basel 1 enhanced geothermal system, Geothermics, 37(5), 469–495.

Heroux, M. A., Phipps, E. T., Salinger, A. G., Thornquist, H. K., Tuminaro, R. S., Willenbring, J. M., Williams, A., Stanley, K. S., Bartlett, R. A., Howle, V. E., Hoekstra, R. J., Hu, J. J., Kolda, T. G., Lehoucq, R. B., Long, K. R., & Pawlowski, R. P., 2005. An overview of the Trilinos project, ACM Transactions on Mathematical Software, 31(3), 397–423.

Herrmann, M., Kraft, T., Tormann, T., Scarabello, L., & Wiemer, S., 2019. A Consistent High-Resolution Catalog of Induced Seismicity in Basel Based on Matched Filter Detection and Tailored Post-Processing, Journal of Geophysical Research: Solid Earth, 124(8), 8449–8477.

Hirschberg, S., Wiemer, S., & Burgherr, P., 2015. Energy from the Earth: Deep Geothermal as a Resource for the Future?.

Jefferson W. Tester Brian J. Anderson, A. S. B. D. D. B. R. D. E. M. D. J. G. B. L. M. C. M. K. N. S. P. M. N. T. & Jr., R. W. V., 2006. The future of geothermal energy: Impact of enhanced geothermal systems (EGS) on the United States in the 21st century, report, MIT.

Jin, L. & Zoback, M. D., 2017. Fully Coupled Nonlinear Fluid Flow and Poroelasticity in Arbitrarily Fractured Porous Media: A Hybrid-Dimensional Computational Model, Journal of Geophysical Research: Solid Earth, 122(10), 7626–7658.

Kanamori, H., 1977. The energy release in great earthquakes.

Karvounis, D. C., 2013. Simulations of enhanced geothermal systems with an adaptive hierarchical fracture representation.

Karvounis, D. C. & Jenny, P., 2016. Adaptive Hierarchical Fracture Model for Enhanced Geothermal Systems, Multiscale Modeling & Simulation, 14(1), 207–231.

Karvounis, D. C., Gischig, V. S., & Wiemer, S., 2014. Towards a Real-Time Forecast of Induced Seismicity for Enhanced Geothermal Systems, in Shale Energy Engineering 2014, pp. 246–255, American Society of Civil Engineers, Reston, VA.

Kim, K.-H., Ree, J.-h., Kim, Y., Kim, S., Kang, S. Y., & Seo, W., 2018. Assessing whether the 2017 M w 5.4 Pohang earthquake in South Korea was an induced event, Science, 360(6392), 1007–1009.

Király-Proag, E., Zechar, J. D., Gischig, V., Wiemer, S., Karvounis, D., & Doetsch, J., 2016. Validating induced seismicity forecast models-Induced Seismicity Test Bench, Journal of Geophysical Research: Solid Earth, 121(8), 6009–6029.

Király-Proag, E., Gischig, V., Zechar, J. D., & Wiemer, S., 2018. Multicomponent ensemble models to forecast induced seismicity, Geophysical Journal International, 212(1), 476–490.

Kohl, T. & Mégel, T., 2007. Predictive modeling of reservoir response to hydraulic stimula-

tions at the European EGS site Soultz-sous-Forêts, International Journal of Rock Mechanics and Mining Sciences, 44(8), 1118–1131.

Kraft, T. & Deichmann, N., 2014. High-precision relocation and focal mechanism of the injection-induced seismicity at the Basel EGS, Geothermics.

Langenbruch, C., Weingarten, M., & Zoback, M. D., 2018. Physics-based forecasting of man-made earthquake hazards in Oklahoma and Kansas, Nature Communications, 9(1), 3946.

Lee, K.-K., Ellsworth, W. L., Giardini, D., Townend, J., Ge, S., Shimamoto, T., Yeo, I.-W., Kang, T.-S., Rhie, J., Sheen, D.-h., Chang, C., Woo, J.-U., & Langenbruch, C., 2019. Managing injection-induced seismic risks, Science, 364(6442), 730–732.

Lemonnier, P. & Bourbiaux, B., 2010. Simulation of Naturally Fractured Reservoirs. State of the Art, Oil & Gas Science and Technology – Revue de l'Institut Français du Pétrole, 65(2), 239–262.

Li, S., Feng, X. T., Zhang, D., & Tang, H., 2019. Coupled thermo-hydro-mechanical analysis of stimulation and production for fractured geothermal reservoirs, Applied Energy, 247(December 2018), 40–59.

Liao, J., Hou, Z., Haris, M., Tao, Y., Xie, Y., & Yue, Y., 2020. Numerical evaluation of hot dry rock reservoir through stimulation and heat extraction using a three-dimensional anisotropic coupled THM model, Geothermics, 83(September 2019), 101729.

Llanos, E. M., Zarrouk, S. J., & Hogarth, R. A., 2015. Numerical model of the Habanero geothermal reservoir, Australia, Geothermics, 53, 308–319.

McClure, M. W. & Horne, R. N., 2011. Investigation of injection-induced seismicity using a coupled fluid flow and rate/state friction model, in GEOPHYSICS, vol. 76, pp. WC181–WC198.

McClure, M. W. & Horne, R. N., 2014. An investigation of stimulation mechanisms in Enhanced Geothermal Systems, International Journal of Rock Mechanics and Mining Sciences, 72, 242–260.

McGarr, A., 1976. Seismic moments and volume changes, Journal of Geophysical Research, 81(8), 1487–1494.

Meier, P. M., Rodríguez, A., & Bethmann, F., 2015. Lessons Learned from Basel: New EGS Projects in Switzerland Using Multistage Stimulation and a Probabilistic Traffic Light System for the Reduction of Seismic Risk, Proceedings World Geothermal Congress, (April), 19–25.

Mena, B., Wiemer, S., & Bachmann, C., 2013. Building Robust Models to Forecast the

Induced Seismicity Related to Geothermal Reservoir Enhancement, Bulletin of the Seismological Society of America, 103(1), 383–393.

Mignan, A., Landtwing, D., Kästli, P., Mena, B., & Wiemer, S., 2015. Induced seismicity risk analysis of the 2006 Basel, Switzerland, Enhanced Geothermal System project: Influence of uncertainties on risk mitigation, Geothermics, 53.

Mignan, A., Broccardo, M., Wiemer, S., & Giardini, D., 2017. Induced seismicity closed-form traffic light system for actuarial decision-making during deep fluid injections, Scientific Reports, 7(1), 1–10.

Mignan, A., Karvounis, D., Broccardo, M., Wiemer, S., & Giardini, D., 2019. Including seismic risk mitigation measures into the Levelized Cost Of Electricity in enhanced geothermal systems for optimal siting, Applied Energy, 238, 831–850.

Mourzenko, V., Thovert, J.-F., & Adler, P., 2005. Percolation of three-dimensional fracture networks with power-law size distribution, Physical Review E, 72(3), 036103.

Murphy, A. H. & Winkler, R. L., 1987. A General Framework for Forecast Verification, Monthly Weather Review, 115(7), 1330–1338.

Oda, M., 1985. Permeability tensor for discontinuous rock masses, Géotechnique, 35(4), 483–495.

Ogata, Y., 1999. Seismicity Analysis through Point-process Modeling: A Review, in Seismicity Patterns, their Statistical Significance and Physical Meaning, pp. 471–507, Birkhäuser Basel, Basel.

Olasolo, P., Juárez, M. C., Morales, M. P., Damico, S., & Liarte, I. A., 2016. Enhanced geothermal systems (EGS): A review, Renewable and Sustainable Energy Reviews, 56, 133–144.

Olivella, S., Carrera, J., Gens, a., & Alonso, E. E., 1994. Nonisothermal multiphase flow of brine and gas through saline media, Transport in Porous Media, 15(3), 271–293.

Ortiz R., A. E., Renner, J., & Jung, R., 2011. Hydromechanical analyses of the hydraulic stimulation of borehole Basel 1, Geophysical Journal International, 185(3), 1266–1287.

O'Sullivan, M. J. & O'Sullivan, J. P., 2016. Reservoir modeling and simulation for geothermal resource characterization and evaluation, Elsevier Ltd.

Peaceman, D. W., 1978. Interpretation of Well-Block Pressures in Numerical Reservoir Simulation(includes associated paper 6988), Society of Petroleum Engineers Journal, 18(3), 183–194.

Peacock, D. C., Nixon, C. W., Rotevatn, A., Sanderson, D. J., & Zuluaga, L. F., 2016. Glossary of fault and other fracture networks, Journal of Structural Geology, 92, 12–29.

Pritchett, J. W., 2015. Development of an Advanced Stimulation / Production Predictive Simulator for Enhanced Geothermal Systems, Tech. rep., Golden Field Office, Golden, CO (United States).

Riffault, J., Dempsey, D., Karra, S., & Archer, R., 2018. Microseismicity Cloud Can Be Substantially Larger Than the Associated Stimulated Fracture Volume: The Case of the Paralana Enhanced Geothermal System, Journal of Geophysical Research: Solid Earth, 123(8), 6845–6870.

Rinaldi, A. P. & Nespoli, M., 2017. TOUGH2-seed: A coupled fluid flow and mechanical-stochastic approach to model injection-induced seismicity, Computers and Geosciences, 108(June 2016), 86–97.

Rinaldi, A. P., Vilarrasa, V., Rutqvist, J., & Cappa, F., 2015. Fault reactivation during CO 2 sequestration: Effects of well orientation on seismicity and leakage, Greenhouse Gases: Science and Technology, 5(5), 645–656.

Russell, T., 1989. Stability Analysis and Switching Criteria for Adaptive Implicit Methods Based on the CFL Condition, in SPE Symposium on Reservoir Simulation, Society of Petroleum Engineers.

Rybach, L., 2010. " The Future of Geothermal Energy " and Its Challenges, Proceedings World Geothermal Congress 2010, (April), 2006–2009.

Sanyal, S. K., Butler, S. J., Swenson, D., & Hardeman, B., 2000. Review of the state-of-the-art of numerical simulation of Enhanced Geothermal Systems, in Proceedings World Geothermal Congress 2000, Kyushu - Tohoku, Japan, May 28 - June 10, 2000.

Schill, E., Genter, A., Cuenot, N., & Kohl, T., 2017. Hydraulic performance history at the Soultz EGS reservoirs from stimulation and long-term circulation tests, Geothermics, 70, 110–124.

Shapiro, S. A. & Dinske, C., 2009. Scaling of seismicity induced by nonlinear fluid-rock interaction, Journal of Geophysical Research, 114(B9), B09307.

Shapiro, S. A., Dinske, C., Langenbruch, C., & Wenzel, F., 2010. Seismogenic index and magnitude probability of earthquakes induced during reservoir fluid stimulations, The Leading Edge, 29(3), 304–309.

Thomas, G. & Thurnau, D., 1983. Reservoir Simulation Using an Adaptive Implicit Method, Society of Petroleum Engineers Journal, 23(05), 759–768.

Trutnevyte, E. & Wiemer, S., 2017. Tailor-made risk governance for induced seismicity of geothermal energy projects: An application to Switzerland, Geothermics, 65, 295–312.

Ucar, E., Berre, I., & Keilegavlen, E., 2018. Three-Dimensional Numerical Modeling of Shear

Stimulation of Fractured Reservoirs, Journal of Geophysical Research: Solid Earth, 123(5), 3891–3908.

Valley, B. & Evans, K. F., 2009. Stress orientation to 5 km depth in the basement below Basel (Switzerland) from borehole failure analysis, Swiss Journal of Geosciences, 102(3), 467–480.

Vallier, B., Magnenet, V., Schmittbuhl, J., & Fond, C., 2019. Large scale hydro-thermal circulation in the deep geothermal reservoir of Soultz-sous-Forêts (France), Geothermics, 78(December 2018), 154–169.

van der Elst, N. J., Page, M. T., Weiser, D. A., Goebel, T. H., & Hosseini, S. M., 2016. Induced earthquake magnitudes are as large as (statistically) expected, Journal of Geophysical Research: Solid Earth, 121(6), 4575–4590.

Vitel, S. & Souche, L., 2007. Unstructured Upgridding and Transmissibility Upscaling for Preferential Flow Paths in 3D Fractured Reservoirs, in Proceedings of SPE Reservoir Simulation Symposium, pp. 1–11, Society of Petroleum Engineers.

Wang, Y., Li, T., Chen, Y., & Ma, G., 2019. A three-dimensional thermo-hydro-mechanical coupled model for enhanced geothermal systems (EGS) embedded with discrete fracture networks, Computer Methods in Applied Mechanics and Engineering, 356, 465–489.

Wassing, B., van Wees, J., & Fokker, P., 2014. Coupled continuum modeling of fracture reactivation and induced seismicity during enhanced geothermal operations, Geothermics, 52, 153–164.

White, M., Fu, P., McClure, M., Danko, G., Elsworth, D., Sonnenthal, E., Kelkar, S., & Podgorney, R., 2018. A suite of benchmark and challenge problems for enhanced geothermal systems, Geomechanics and Geophysics for Geo-Energy and Geo-Resources, 4(1), 79–117.

Yeck, W. L., Hayes, G. P., McNamara, D. E., Rubinstein, J. L., Barnhart, W. D., Earle, P. S., & Benz, H. M., 2017. Oklahoma experiences largest earthquake during ongoing regional wastewater injection hazard mitigation efforts, Geophysical Research Letters, 44(2), 711–717.

Yoo, H., Park, S., Xie, L., Kim, K. I., Min, K. B., Rutqvist, J., & Rinaldi, A. P., 2021. Hydro-mechanical modeling of the first and second hydraulic stimulations in a fractured geothermal reservoir in Pohang, South Korea, Geothermics, 89, 101982.

Zarrouk, S. J. & Moon, H., 2014. Efficiency of geothermal power plants: A worldwide review, Geothermics, 51, 142–153.

Zbinden, D., Rinaldi, A. P., Diehl, T., & Wiemer, S., 2020. Potential influence of overpressurized gas on the induced seismicity in the St. Gallen deep geothermal project (Switzerland),

Solid Earth, 11(3), 909–933.

Ziegler, M., Valley, B., & Evans, K. F., 2015. Characterisation of Natural Fractures and Fracture Zones of the Basel EGS Reservoir Inferred from Geophysical Logging of the Basel-1 Well, Proceedings World Geothermal Congress 2015, (April), 19–25.

Ţene, M., Bosma, S. B., Kobaisi, M. S. A., & Hajibeygi, H., 2017. Projection-based Embedded Discrete Fracture Model (pEDFM), Advances in Water Resources.

Table A1. Materials' hydraulic and geological properties

Property	Value
Working fluid (water)	
Density ρ	1000 kg/m^3
Viscosity μ	0.001 $s \cdot Pa$
Specific heat capacity c_h	4183 $J/(kg \cdot K)$
Hot solids (granite)	
Density ρ^r	2700 kg/m^3
Heat conductivity $\hat{\mathbf{\Lambda}}$	2.5 $W/(m \cdot K)$
Specific heat capacity c_h^r	2600 $J/(kg \cdot K)$
Effective fractured reservoir ($t \leq 0$)	
Porosity of the damaged matrix ϕ_0^d	0.01
Permeability of the damaged matrix k^d	$2. \cdot 10^{-17}$ m^2
Fracture density $\ddot{\rho}_f$	0.4 m^{-1}
Fracture compressibility α	$1.8 \cdot 10^{-10}$ mPa^{-1}
Principal stresses	(Häring et al., 2008)
$\langle \lvert \boldsymbol{\sigma}_1 \rvert \rangle$	144. MPa
$\langle \lvert \boldsymbol{\sigma}_2 \rvert \rangle$	117. MPa
$\langle \lvert \boldsymbol{\sigma}_3 \rvert \rangle$	69. MPa
Formation's pressure $p(t < 0), \forall \mathbf{x} \in \Omega$	45 MPa
Open cased well segment	
Well compressibility $[m^2/Pa]$	$9 \cdot 10^{-11}$
Well radius (constant) $[m]$	0.12
Bottom of the 1st well	$(0, 0, -5000)$ m
Important pre-stimulated discrete fracture Ω_1^f (section 5)	
Mechanical aperture $b_{m,1}^1$ $[\mu m]$	500.μm
Hydraulic aperture b_h^1 $[\mu m]$	100.μm
Disc centred at	$(39, -17, -46755)$ m
with strike	200°,
dip	26°, and
radius	22. m

Table A2. Common modelling DFHM parameters

Property	Value
Stochastic modelling	
b-value of Gutenberg-Richter law	1.3
Range $[M_{min},\ M_{max})$	$[0.6\ ,\ 7.5)$
Stress drop $\Delta\tau$	2.32 MPa
Cohesion C_0	2 MPa
Friction coefficient μ	0.6
Standard deviation of $\lvert\sigma_i\rvert,\ i = \{1, 2, 3\}$	$0.2 \cdot \langle\sigma_i\rangle$
Deterministic modelling	
Damaged matrix discretisation length Δx^d	40 m
Fractures' discretisation length Δx^f	≈ 20 m
Time step power law coefficient Δt	100 s
Time step power law exponent	0.25
Depth of casing shoe	4.632 km
Well model	as in Peaceman (1978)
AIM stencil	$27-$points stencil
Updating deterministic flow model	
Minimum discrete fracture radius R_{min}	25 m
Initial mechanical aperture $b^i_{m,0}$	0.125 mm
Post-rupture mechanical aperture b^f	1 mm
Post-rupture permeability k^f (for 0.2 mm hydraulic aperture)	$3.\bar{3} \cdot 10^{-9}\ m^2$ $\left(= {}^{0.0002^2}/_{12}\right)$

Table A3. Variable DFHM parameters

Modelling parameter	40 years doublet (section 4.1)	abandoned well (section 4.2)	Monte Carlo DHFM simulation (section 5)
Sets of seeds	2	1	1
Total density of seeds $\dot{\rho}_s$	$\approx 10^6$[seeds/km^3]	$\approx 10^6$[seeds/km^3]	$\approx 5 \cdot 10^5$[seeds/km^3]
Orientation of 1st set	uniform in $[0, 4\pi]$	uniform in $[0, 4\pi]$	uniform in $[0, 4\pi]$
Orientation of 2nd set	uniform, but at most 35^o from direction $(\boldsymbol{\sigma}_1 + \boldsymbol{\sigma}_3)$	—	—
Critical friction $\delta\mu$	0.05	0.001	0.05
1st principal stress direction	$(1, 0, 0)$	$(1, 0, 0)$	$(0.5878, -0.80902, 0)$
2nd principal stress direction	vertical	vertical	vertical
For the 3rd stress direction, orthogonality is assumed: $\boldsymbol{\sigma}_3 = \boldsymbol{\sigma}_2 \times \boldsymbol{\sigma}_1$			
Orientation of well segment	vertical	vertical	as in BS1 (Häring et al., 2008)